energies

Review

Application of Operando X-ray Diffractometry in Various Aspects of the Investigations of Lithium/Sodium-Ion Batteries

Wen Zhu, Yuesheng Wang, Dongqiang Liu, Vincent Gariépy, Catherine Gagnon, Ashok Vijh, Michel L. Trudeau and Karim Zaghib *

Centre d'excellence en électrification des Transports et Stockage d'énergie, 1806 Lionel Boulet, Varennes, QC J3X 1S1, Canada; Zhu.Wen@ireq.ca (W.Z.); Wang.Yuesheng@ireq.ca (Y.W.); Liu.Dongqiang@ireq.ca (D.L.); Gariepy.Vincent@ireq.ca (V.G.); Gagnon.Catherine@ireq.ca (C.G.); Vijh.Ashok@ireq.ca (A.V.); Trudeau.Michel@ireq.ca (M.L.T.)

* Correspondence: zaghib.karim@ireq.ca, Tel.: +1-450-652-8019

Received: 28 September 2018; Accepted: 24 October 2018; Published: 1 November 2018

Abstract: The main challenges facing rechargeable batteries today are: (1) increasing the electrode capacity; (2) prolonging the cycle life; (3) enhancing the rate performance and (4) insuring their safety. Significant efforts have been devoted to improve the present electrode materials as well as to develop and design new high performance electrodes. All of the efforts are based on the understanding of the materials, their working mechanisms, the impact of the structure and reaction mechanism on electrochemical performance. Various operando/in-situ methods are applied in studying rechargeable batteries to gain a better understanding of the crystal structure of the electrode materials and their behaviors during charge-discharge under various conditions. In the present review, we focus on applying operando X-ray techniques to investigate electrode materials, including the working mechanisms of different structured materials, the effect of size, cycling rate and temperature on the reaction mechanisms, the thermal stability of the electrodes, the degradation mechanism and the optimization of material synthesis. We demonstrate the importance of using operando/in-situ XRD and its combination with other techniques in examining the microstructural changes of the electrodes under various operating conditions, in both macro and atomic-scales. These results reveal the working and the degradation mechanisms of the electrodes and the possible side reactions involved, which are essential for improving the present materials and developing new materials for high performance and long cycle life batteries.

Keywords: operando/in-situ XRD; olivine structure; layered metal oxide; spinel oxide; tunnel-type structure

---

1. Introduction

Lithium-ion batteries (LIBs) have been widely used because of their relatively high energy/power densities, long cycle life and slow self-discharge, whereas sodium-ion batteries (SIBs) are considered as low cost alternatives for large-scale energy storage systems. To fulfil the demands of energy storage in the transportation and power utility industries, batteries with high energy density and long cycle life are needed. Therefore, it is critical to improve present electrode and electrolyte materials as well as develop new ones for obtaining high quality batteries [1–3]. The known electrode materials are classified into three main categories: (a) insertion type, including layered oxides (LM_TO_2, $Na_xM_TO_2$, M_T = transition metal(s)); spinel oxides ($LiM_{T2}O_4$), tunnel type oxides ($Na_xM_TO_2$) and polyanionic compounds (Li/NaM_TPO_4, $Na_3V_2(PO_4)_3$, $Na_2F_2(SO_4)_3$); (b) conversion type (S, MF, MCl, M = metal) and (c) alloying type, (Si, Sn and intermetallic compounds) [4–6].

LiM_TO_2 layered oxides, including $LiCoO_2$ (LCO), $LiNi_{1-x-y}Mn_xCo_yO_2$ (NMC) and Li_2MnO_3-NMC, have high capacity, high voltage, long cycling life and good rate performance, which are widely used in the consumer electronics and electrical vehicles, but these materials show high initial reversible capacity loss, low thermal stability and reduced safety as well as high cost [5,7–10]. Spinel $LiM_{T2}O_4$ compounds (M_T = Mn, Mn+Ni) have high energy density, high voltage and low cost, but their cycling life at high rates is insufficient for practical applications [11–14]. $LiFePO_4$ is the best known in the LiM_TPO_4 family with its low cost and high safety despite its low potential among the family members (M_T = Mn, Co and Ni) [15–20].

$Na_xM_TO_2$ compounds are the promising cathode materials for SIBs. Single-transition metal P2-$Na_xM_TO_2$ oxides (see Section 3.1.2 for P2 and O3 structure information) have high ionic conductivity, high capacity and high potential, but poor capacity retention [4]. As a result, various multi-transition metal P2-$Na_xM_TO_2$ compounds, such as P2-$Na_{0.66}Ni_{0.34}Mn_{0.66}O_2$ and P2-$Na_{0.68}Cu_{0.34}Mn_{0.66}O_2$, are developed to enhance the capacity retention. Multi-transition metal O3-$Na_xM_TO_2$ oxides, e.g., $Na_{0.9}Ni_{0.4}Mn_xTi_{0.6-x}O_2$ and $Na_{0.9}Cu_{0.22}Mn_{0.48}Fe_{0.3}O_2$, have relatively high reversible capacities and good retentions [21,22]. Among the poly-anionic compounds, nano-maricite $NaFePO_4$ has a high reversible capacity and capacity retention [23]. In addition, NASICON structured $Na_3V_2(PO_4)_3$ and $Na_4M_TV(PO_4)_3$ possess reversible capacities $\geq$100 mAh g^{-1} and good capacity retentions [24,25].

Graphite carbon is a low cost anode material used in commercial LIBs with its moderate energy/power densities and long cycle life despite its interaction with a propylene carbonate-based electrolyte [26] and ~10% uniaxial change along c-axis [5]. Unfortunately, it shows poor electrochemical Na^+ storage with the carbonate electrolyte. Hard carbon is considered as a promising anode for SIBs, its nanoparticles and nano-voids lead to reduced and isotropic volume expansion as well as excess gravimetric capacity [5,27,28]. Spinel $Li_4Ti_5O_{12}$ is another anode material, its "zero strain" character in LIBs allows high rate and long cycle life; but it reacts with organic electrolyte [29,30]. Recently, new anode materials, such as expanded graphite [31,32], ReS_2 [33], textured TiO_2 nanotube [34] and N-doped Fe3C@C/Se [35], have been studied, which show high capacities.

The electrolyte is an important factor determining cell stability, cycle life and safety for all batteries [36–40]. Electrolytes are classified as: (a) non-aqueous liquids (e.g., carbonate-based electrolytes; ionic liquids) (b) polymers (e.g., polyethylene oxide (PEO)); (c) ceramics (e.g., $Li_7La_3Zr_2O_{12}$, $K_2Fe_4O_7$); and (d) aqueous solutions. Organic solvent-based electrolytes are widely used in rechargeable batteries, but safety concerns arise from their flammable, volatile and toxic natures. Ionic liquids [36,41–44] are proposed as alternatives to solve the flammability problem, but with a high cost. Recently, great effort is being devoted to "all solid" batteries, polymer electrolytes, PEO [36,45–47], having become one of the promising choices. In addition, garnet-type $Li_7La_3Zr_2O_{12}$ with its room temperature ion conductivity of 10^{-4} S cm^{-1} has also attracted a lot of attention [48–50].

Currently, although many materials are studied as electrodes for LIBs and SIBs, only a few are used in commercial batteries because most of them cannot meet the requirements of practical applications. Even the batteries already on the market still need improvement, especially the cycle life, which is a function of cycle rate, cycle voltage and environment. The ultimate cause of capacity fade is the microstructure changes of the electrode materials during cycling, such as formation of a solid electrolyte interface, irreversible phase transformation, and the impact of phase transition on capacity retention of different materials. Thus, it is essential to understand the reaction mechanisms of electrode materials under various conditions in order to ameliorate their performance.

A better understanding of the working and capacity fade mechanisms of batteries is the key to improve their properties and increase cycle life. Various ex-situ material characterization techniques are used to examine the pristine and cycled electrodes; among them, X-ray diffraction (XRD) and neutron diffraction (ND) are two of the most important techniques to analyze and determine the structure change of the crystalline phases in the electrode materials [51–53]. However, the ex-situ methods cannot provide real-time information of the electrodes during cycling, which is indispensable for the comprehension of the working and degradation mechanisms of the batteries. The characterization techniques have advanced significantly in the past few years, with operando/in-situ (operando and in-situ will be used interchangeably hereafter) methods widely applied in monitoring the real-time dynamics of electrodes in batteries under various operating conditions. The phase transformation and crystal structure change during cycling are investigated via operando XRD [12,54–60] and operando ND [61–65]. The former is widely used because of equipment availability and relatively simple operating procedures; in contrast, ND is not as popular due to the expensive neutron sources and high maintenance cost, despite its advantage of high penetration, high signal-to-noise ratio and high sensitivity to the light elements (such as lithium) as compared to XRD. Operando X-ray diffraction-computed tomography (XRD-CT) [66] and operando hard X-ray microscopy [67] are employed to track space-resolved information, the former probes the crystal structures and transformations at millimeter scale, whereas the latter reveals the dynamic phase transformation process on both single and multi-particles. The diffraction technique measures the collective properties of the electrode, whereas the complimentary information of the local and surface/interface structures, such as the oxidation state of ions, coordination number, average interatomic distances, and electronic configuration changes during the electrochemical process are obtained by operando X-ray absorption spectroscopy (XAS) [68–73], Raman spectroscopy [74–78] and Fourier-transform infrared (FTIR) [79–82]. The electrode changes occurring under working conditions are also observed via operando scanning electron microscopy (SEM) [83–85] and (scanning) transmission electron microscopy ((S)TEM) [86–91] at the micro- and nano-scales and analyzed with energy dispersive X-ray spectroscopy (EDS), electron energy loss spectroscopy (EELS) and electron diffraction. The information on crystal structure, phase transformation, multi-phase interface behavior, element location and distribution are revealed by operando measurements or multi-operando measurements, which enable researchers to understand the operation and failure mechanisms of electrodes as well as to improve the structure of the materials and enhance the performance of the batteries. Of all the operando techniques, X-ray diffraction is the most widely used due to readily availability of the instrument, simple cell design and the ability to: (1) resolve crystal structure and follow phase transformations [92–100]; (2) determine stress induced in electrodes during cycling [101]; (3) probe thermal stability [102–105]; (4) monitoring phase formation during heat treatments and provide information on the optimization of synthesis processes [106,107]. In the present work, we focus on the recent advances in operando XRD to explore the reaction mechanisms of lithium and sodium electrode materials with olivine structure, layered structure, spinel structure, tunneled structure, as well as to study the thermal stability of the electrodes and material synthesis process.

2. Operando X-ray Diffraction Technique

The operando XRD, both reflection and transmission modes are used to monitor crystal structure change and phase transitions of electrodes during the electrochemical process. Various in-situ cells were designed [108–114] with X-ray transparent windows, such as a beryllium disk [54,104,115], polymer films (Kapton, Mylar) [116,117] and aluminum foil [109,110]. A beryllium window has the advantages of maintaining contact between cell components and is nearly 100% X-ray transparent due to the rigidity of the metal disk and low X-ray absorption. However, beryllium corrosion was observed at voltage > 4.2 V [54,118], and it is toxic and expensive. On the other hand, Kapton, Mylar and aluminum are stable, low cost and non-toxic. They also allow X-rays to pass through with certain absorption, but it is difficult to keep cells with a large area window pressurized due to their flexibility. Aluminum foil is used as a current collector in many cases; the same aluminum foil is also used as an X-ray window to reduce undesired diffraction peaks in the spectra. The evolution of both cathode and anode can be monitored simultaneously via high-energy synchrotron X-rays in transmission mode [112,114,119–122].

3. The Operando XRD Studies in Li^+/Na^+ Batteries

3.1. Reaction Mechanisms

3.1.1. Olivine Structured Cathodes of $LiFePO_4$ and $NaFePO_4$

1. $LiFePO_4$

$LiFePO_4$ (LFP) is a promising cathode material with reasonable high capacity, superior cycle-life, structural and thermal stability, as well as low cost, non-toxicity and high safety despite its low operating voltage and low conductivity [123–125]. LFP and its charging end product $FePO_4$ (FP) have olivine structure, with orthorhombic unit cell and *Pnma* space group (S.G.). Lithium-ion intercalation and de-intercalation occur in one dimensional channels along the [010] direction [91,126,127]. The two-phase reaction mechanism was first proposed due to the very narrow single-phase range near the stoichiometry compositions of $Li_{1\text{-}\beta}FePO_4$ and $Li_\alpha FePO_4$, with β and α varying from 0.032–0.05 and 0.032–0.11 at room temperature, respectively [128–130]. The two-phase mechanism with LFP and FP domains that are separated by a phase boundary is supported by both ex-situ and in-situ TEM observations [91,131,132] and in-situ XRD results [16,100,133,134]. Detailed studies on the $LiFePO_4$ to $FePO_4$ transition demonstrate that the reaction mechanism not only depends on the material intrinsic properties, but also depends on the particle size and orientation [135–139], the cycling rate [140,141] and the strain [142,143] etc. Thus, the two-phase reaction is only applicable under certain conditions. Operando XRD is employed to explore the LFP–FP phase transformation mechanisms and their relation to material properties and operating conditions.

- The working mechanism of LFP under the quasi-equilibrium condition

In-situ XRD was conducted on LFP cycled at a low current of 2.3 mA g^{-1}, which is close to the thermodynamic equilibrium condition [133]. Figure 1a shows that the starting cathode contains only LFP, but FP starts to form and grow as charge proceeds; only a small amount of LFP is left at the end of charge. During discharge, the LFP peaks grow at the expense of FP, and no FP peaks are observed at the end of discharge. The cycling is reversible, and only LFP and FP are observed, which is consistent with the two-phase reaction mechanism. In addition, the two-phase mechanism is also supported by in-situ high resolution TEM (HRTEM), Figure 1b–d show the migration of the phase boundary between FP and LFP along the [010] direction during lithiation and the dislocations induced at the phase boundary [91].

- The effect of particle size on the working mechanism

Meethong et al. [144] studied the size-effect on the lithium miscibility gap in $Li_{1-\beta}FePO_4$ at slow rate of C/50, and found the gap shrank as the particle size decreased. The solid-solution limits β and α ($Li_\alpha FePO_4$) increased from ~0.03 to ~0.12 and ~0.01 to ~0.12, respectively, as the average particle size varied from 113 to 34 nm; similar results are obtained via neutron diffraction and theoretical calculation [138]. These results suggest that the phase transformation mechanism with small particles may be different from large particles, and operando XRD measurements have confirmed this proposal. Li et al. [137] monitored the phase transformations of [100] oriented LFP cathodes with three thicknesses in the [100] direction at a rate of C/5. Figure 2 focuses on the characteristic peaks (020)/(211) of LFP and FP.

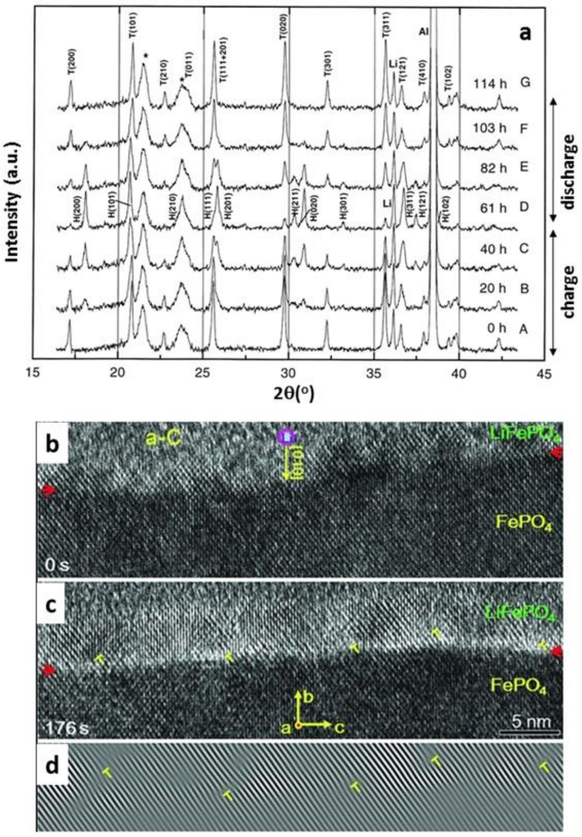

Figure 1. (**a**) XRD spectra collected during the first galvanostatic cycle between 4.0 and 2.9 V. T:$LiFePO_4$; H:$FePO_4$; *: cell package [133]. (**b**) HRTEM image of phase boundary (marked by red arrows) between FP and LFP along the [010] direction during lithiation; time = 0 s. (**c**) At 176 s, the thickness of the LFP layer increased. (**d**) Inverse fast Fourier transform (IFFT) image of (**b**), showing the distribution of dislocations near the phase boundary [91]. (**a**) with permission from Elsevier; (**b**–**d**) with permission from the author.

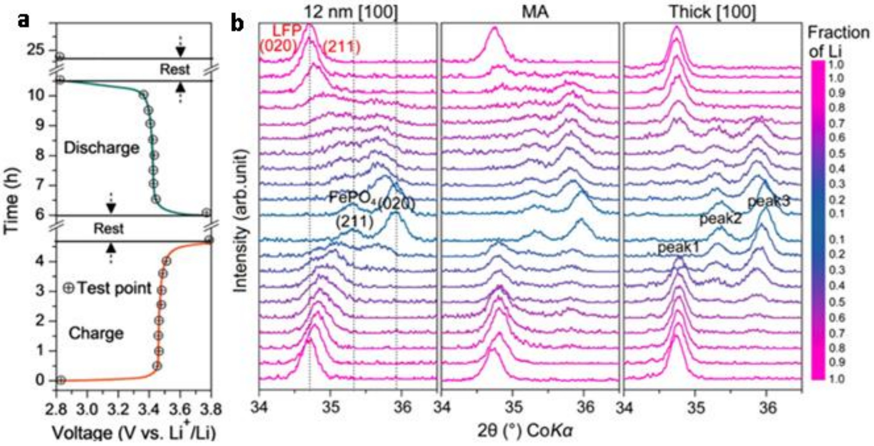

Figure 2. (**a**) Charge/discharge galvanostatic data at 0.2C with the time-points of collecting XRD spectra; (**b**) Operando XRD patterns of coin cells with the 12 nm [100]-LFP, MA-LFP (26 nm), and thick [100]-LFP (46 nm) as cathode materials. For the 12 nm [100]-LFP, a continuous shift of peak1(~34.7°) happens implying a single-phase transformation, whereas the other two have peak2 and peak3, indicating formation of FP with nearly constant composition, which is consistent with the two-phase reaction [137]; with permission from the ACS.

During charge, the (020)/(211) of 12-nm-LFP continuous up shifts. At the end of charge, two peaks labelled as (211) and (020) correspond to FP phase. Upon discharge, the two FP peaks down shift continuously, eventually, the (020)/(211) peaks of LFP return to the initial position at the end of discharge. The continuous shift of the diffraction peaks indicates that the phase transformation is similar to that of the solid solution. For the thick [100]-LFP (46 nm), the positions of the (020)/(211) peaks of LFP are almost unchanged during charge, except for an initial small shift. The (020) and (211) peaks of FP are seen at $Li^+ < \sim 0.7$; they are at nearly constant position until $Li^+ \sim 0.2$, and the upshift of the peaks are observed between $0.1 < Li^+ < 0.2$. The main part of the phase transformation of this thick grain LFP follows a two-phase reaction, whereas the solid solution mechanism plays a role near the stoichiometry LFP and FP owing to the corresponding small solubility regions. This study demonstrates that the LFP-FP transition mechanism changes from two-phase to single-phase transition as the particle size decreases. This single-phase reaction path is also predicated by theoretical calculations under non-equilibrium conditions [145,146] and is evidenced by in-situ XRD measurements, as described below.

- The effect of cycling rate on the working mechanism

The influence of cycling rate on the reaction mechanism was investigated on nano-LFP (average size 186 nm) at rates of 5C–20C [141]. Figure 3a–c show the image plots of diffraction patterns for (200), (211)/(020) and (301) peaks of both LFP and FP with cells cycled at 5C, 10C and 20C, respectively. The positive intensities are clearly seen between LFP-(200) and FP-(200) as well as other diffraction lines, and the intensities increase with cycling rate. These positive intensities indicate the existence of phases with lattice parameters deviating from the stoichiometric values under equilibrium conditions. Figure 3d,e display the image plot and selected diffraction lines collected at 10C rate for multi-cycles. At the beginning of the first charge, all the diffraction peaks of LFP are symmetrical; they start to shift and broaden asymmetrically toward the high two theta direction as charging proceeds, meanwhile the FP phase is seen with broad peaks. At the end of discharge, neither the peak position nor the peak shape of LFP returns to their original states, suggesting the formation of a solid solution with less Li content and smaller unit cell than the initial LFP. These results illustrate that the LFP-FP transition not only depends on particle size, but also on cycling rate which is proportional to the applied current. The phase transition of nano-LFP goes through a non-equilibrium solid-solution path at high rate, which confirms the prediction of suppressing phase separation at high current. The LFP-FP transition occurs through a continuous change in structure instead of forming a distinct FP and avoids major re-arrangement of the crystal structure. This non-equilibrium single-phase transition reduces the stresses induced at the two-phase boundary, and interface energy. Thus, the energy barrier for phase transformation is reduced, which makes the high-rate cycling feasible.

- The effect of temperature on the working mechanism

The many in-depth studies on the LFP↔FP phase transition at room temperature provide a reasonably clear picture of the reaction mechanisms as well as the factors that affect the reaction paths. However, the performance of LFP at low temperature still cannot meet the requirements of many applications; therefore, it is necessary to comprehend the low temperature behavior to enhance battery performance. Yan et al. [147] have probed the phase transformation between −20 °C and 40 °C with operando XRD. Figure 4 demonstrates the evolution of XRD spectra of the nano-LFP (average size ~43 nm) electrodes cycled at 20 °C and 0 °C at three different rates, respectively. At 20 °C with scan rate of 1.4 mV/s, the XRD spectra (Figure 4d) show that the position of the LFP peaks are constant, and their disappearance is accompanied by the appearance of FP peaks during charge. The process is reversed during discharge. The image plots of the diffraction lines show almost no positive intensities between LFP and FP peaks (Figure 4a). This behavior is well-described by the two-phase reaction. As the scan rate is raised to 4.2 mV/s at the same temperature, certain positive intensities can be observed on the image plots in $41.7^\circ < 2\theta < 42.8^\circ$ (Figure 4c), implying the solid-solution mechanism plays a role in the transition. This phenomenon is more obvious when the cell is cycled at 0 °C at the same fast rate. The spectra in Figure 4l show the asymmetrical broadening of (211), (311), (121) reflections; the extreme case is that the (311) peaks of LFP and FP are partially overlapped. These results suggest the existence of intermediate phases with lattice parameters between those of $LiFePO_4$ and $FePO_4$ at equilibrium state. The formation of the intermediate phases at 0 °C is due to the lower Li^+ diffusivity at this temperature. The LFP-FP phase transformation is realized via the solid-solution route which is energetically favorable owing to the reduced interfacial and strain energies at the phase boundary.

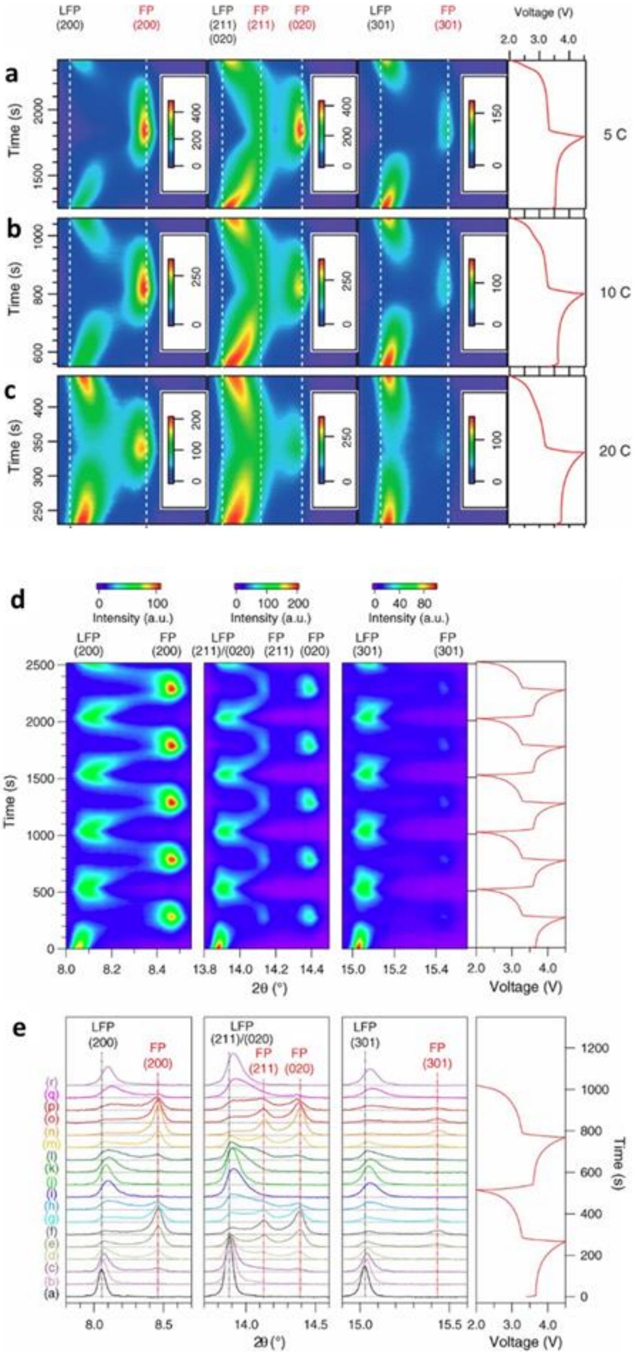

Figure 3. (**a**–**c**) Image plots of operando XRD patterns of LFP collected at 2nd cycle at rates of 5, 10, and 20C. (**d**) Image plots of XRD spectra collected at 10C rate for 5 cycles; (**e**) Selected diffraction patterns during the first two cycles. The corresponding cycling curves are at right of the spectra [141]; with permission from AAAS.

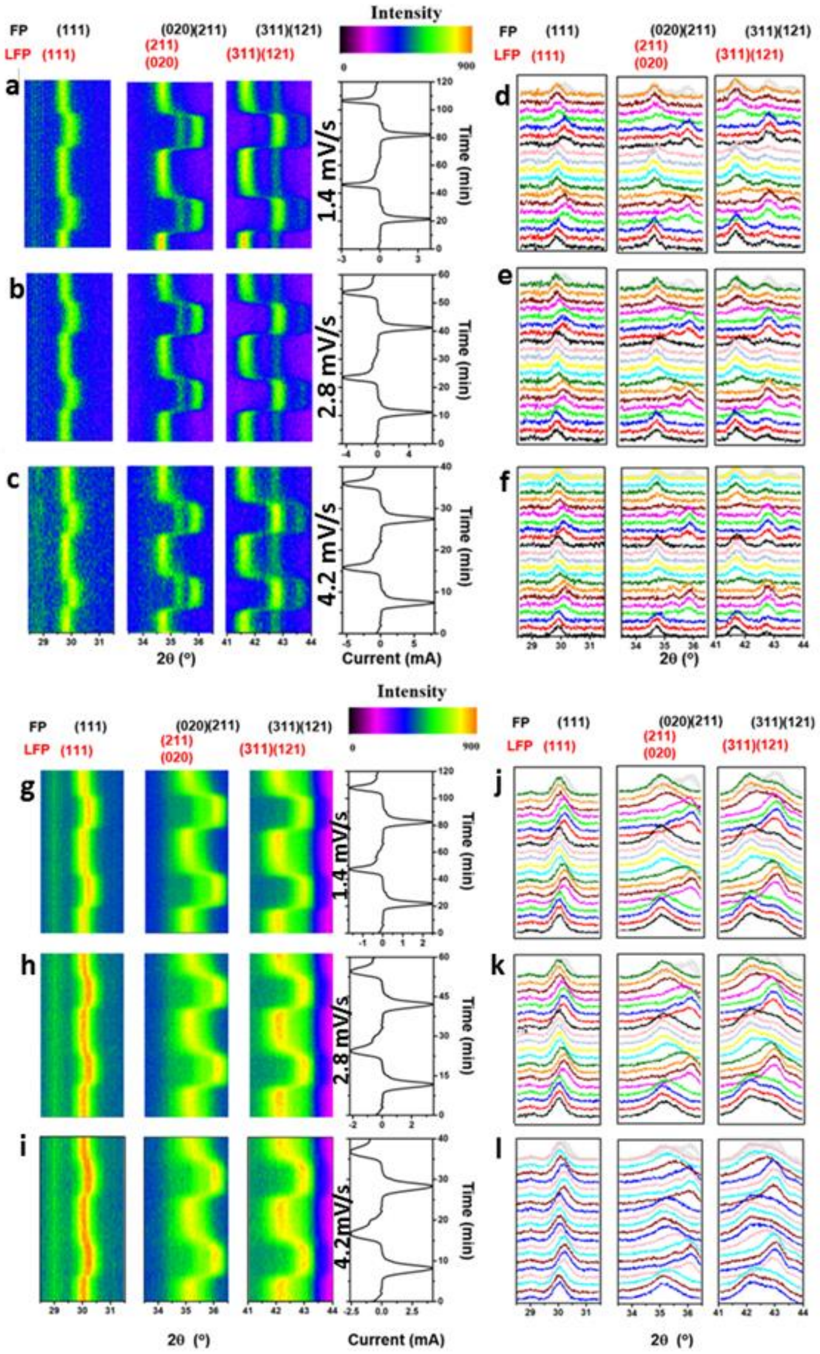

Figure 4. Image plots (**a**–**c**) and corresponding XRD spectra (**d**–**f**) of cells cycled at 1.4, 2.8, and 4.2 mV/s at 20 °C. Image plots (**g**–**i**) and corresponding XRD spectra (**j**–**l**) of cells cycled at 1.4, 2.8, and 4.2 mV/s at 0 °C [147]; with permission from Elsevier.

In summary, the operando XRD measurements have revealed that the phase transformation mechanism of LFP depends on its particle size, the cycling rate/applied current and working temperature. With large particle size, slow cycling rate and relative high temperature(~room temperature), the transformation is dominated by the two-phase mechanism, whereas the solid-solution path is in control with nano-size particles, fast rate and relatively lower temperature (~0 °C).

2. $NaFePO_4$

The understanding of LFP-FP phase transformation is well advanced with many in-depth studies on this system, especially with operando techniques. In contrast, the phase transition of its sodium counterpart, $NaFePO_4$ (NFP), with higher theoretical capacity than other Fe-based poly-anion cathode materials, still needs to be explored in details. Galceran et al. investigated the phase transformation between $NaFePO_4$ and $FePO_4$ with operando XRD [148]. The average particle size of his electrode particles is 800 nm; the in-situ cell is cycled at a rate of C/66, its first cycle results are shown in Figure 5. Figure 5a plots the voltage and Na^+ content versus time, which, unlike LFP, the voltage profile is asymmetrical.

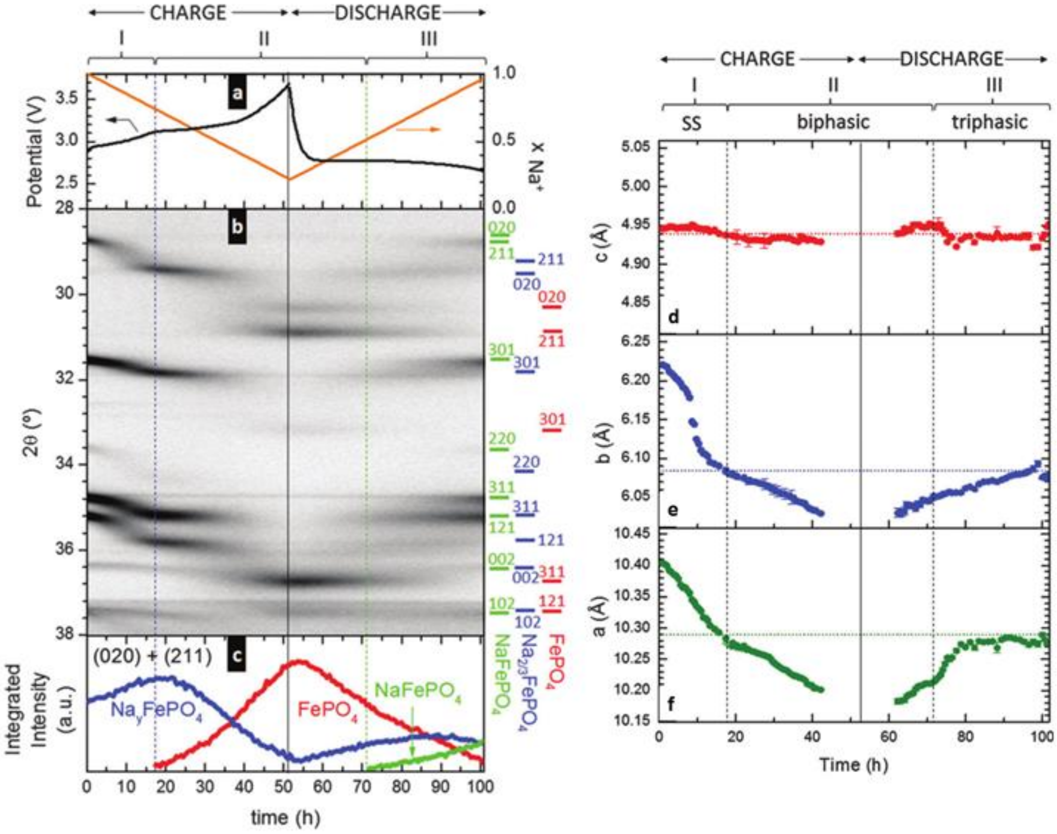

Figure 5. (**a**) Voltage and Na^+ content versus time. (**b**) 2θ versus time plot of the XRD patterns of a full charge-discharge cycle. The grey level is proportional to the relative intensity. Horizontal bars at the right indicate the position of the Bragg peaks for each of the phases. (**c**) Sum of the integrated intensity of the (020) and (211) reflections for each of the phases versus time. (**d**–**f**) The evolution of the cell parameters of Na_xFePO_4 during cycling. The dotted horizontal lines indicate the cell parameters of the chemically synthesized $Na_{2/3}FePO_4$. The solid vertical line indicates end of charge, the two dashed vertical lines separate regions with different mechanisms [148]; with permission from RSC publishing.

Two voltage plateaus, separated by a voltage step at Na^+ ~0.7, are seen on charge, whereas only one plateau is evident on discharge. Figure 5b is the image plot of the XRD spectra with (hkl) of the phases participated labelled on the right axis. At the initial stage of charge, a continuous shift of the $NaFePO_4$ peaks, mostly to the high two theta direction, is observed, which is an indication of a solid-solution reaction; with further extraction of Na ions to Na^+ ~0.7, a new intermediate phase forms, with sodium content ~0.7 and is identified as $Na_{2/3}FePO_4$ [149]. Continuing the extraction of Na^+, $FePO_4$ peaks appear and grow at the expense of the intermediate phase of $Na_{2/3}FePO_4$ until the end of charge. This two-phase reaction continues to hold to the first stage of the discharge process. At this stage, $Na_{2/3}FePO_4$ is formed and increased while $FePO_4$ is consumed. Nevertheless, before reaching mid discharge, $NaFePO_4$ peaks are detected together with the $FePO_4$ and $Na_{2/3}FePO_4$ reflections; upon further discharge of the cell, the $NaFePO_4$ increases mainly at the expenditure of $FePO_4$. Therefore, three phases coexist until the end of discharge. In other words, the charge-discharge cycle can be divided into three stages, labelled as I, II, III at the top of Figure 5a. Stage I follows a solid-solution mechanism, whereas the two-phase reaction mechanism holds in stage II. The solid-solution and two-phase regions are separated at Na^+ ~0.7 during charge, which is in agreement with the phase diagram of olivine $NaFePO_4$ [150], and finally, in stage III, three phases participate the reaction. Figure 5c is a plot of the sum of the integrated intensities of the (020) and (211) peaks of $NaFePO_4$, $Na_\beta FePO_4$ ($0 < \beta < 1$) and $FePO_4$, which act as an indicator of the amount of phase. Figure 5d–f present the evolution of the cell parameters of Na_xFePO_4 during charge and discharge; the sudden change of the lattice parameters corresponds to the change of the reaction mechanisms. The phase transformation mechanism between olivine structured $NaFePO_4$ and $FePO_4$ is different from that of $LiFePO_4 \leftrightarrow FePO_4$; noticeably, the asymmetric reaction path between charge and discharge, and the three-phase reaction during the discharge. In addition, the solid-solution region ($1 \geq Na^+ \geq 0.7$) near stoichiometry $NaFePO_4$ is much greater than that near $LiFePO_4$ under equilibrium conditions. In the $LiFePO_4$ system, the size of the solid-solution region and phase transformation path depends on the particle size and current applied during cycling, as well as temperature, the effects of these factors on the Na^+ solubility in $NaFePO_4$ and phase transition mechanism need to be explored in future studies.

3.1.2. Layer Structured Li_2MoO_3, $Na_x(NiMn)O_2$ and Graphite

Layered oxide, especially the $LiMO_2$ (M = 3d transition metals or their mixture) family, are the most widely used cathode materials in commercial lithium-ion batteries, because of their high voltage and high capacity. $LiCoO_2$ is the first commercialized battery in this family. Many studies are focused on understanding the crystal structure change during cycling, which provide indispensable information for achieving high capacity and long cycling life. Operando XRD investigations revealed the complicated phase transition process involved at least four phases [54,151–155], which cause structure instability; as a consequence, the capacity fades. Adding other transition metals to LCO is found to be effective in suppressing the phase transitions and stabilizing the crystal structure, which lead to another commercial success of $LiNi_{1-x-y}Mn_xCo_yO_2$ series battery with better stability and lower cost. In recent years, sodium-ion batteries have attracted more and more attention due to the concerns with potential shortage of Li resources and high cost for the large-scale energy storage applications [156]. One of the main challenges faced by sodium-ion batteries is the irreversible phase transformation during sodium intercalation and de-intercalation, complicated and often involves several phases, which leads to capacity loss and short cycle life. Here, we focus on the in-situ XRD studies on the phase transformations of the layer structured Li_2MoO_3, Na_xMO_2 cathodes and graphite anode during cycling.

In general, Li/Na_xMO_2 (M = transition metal) layered structures are classified into four groups (P2, O2, O3 and P3) based on the lithium/sodium-ion environment and the number of MO_6 edge-sharing octahedral layers which have three possible positions for the oxygen atoms, named as A, B, C [157]. Figure 6 is a schematic diagram displaying the four crystal structures: (a) O3: **3** different MO_2 layers (BA/CB/AC), Li^+/Na^+ are at ***O***ctahedral sites; (b) P3: **3** different MO_2 layers (BA/AC/CB), Li^+/Na^+ are at trigonal ***P***rismatic sites; (c) O2: **2** different MO_2 layers (BA/CA), Li^+/Na^+ are located at the ***O***ctahedral sites; (d) P2: **2** different MO_2 layers (BA/AB), Li^+/Na^+ are at trigonal ***P***rismatic sites.

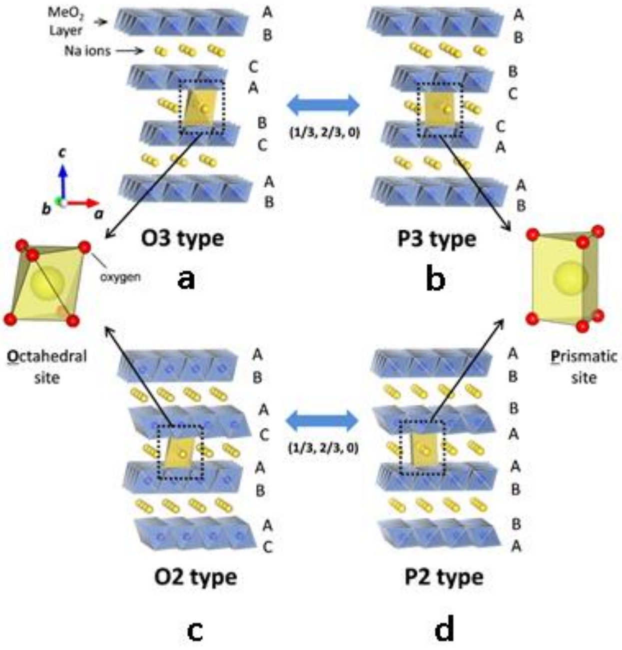

Figure 6. Schematic of the crystal structures for layered Na_xMO_2: (**a**) O3-type; (**b**) P3-type; (**c**) O2- type; (**d**) P2-type. Li/Na: yellow; transition metal: blue; O: red [158], with permission from IOP Publishing.

1. Li_2MoO_3

Many layered cathode materials have an O3-typed stacking, including the widely used and studied $LiMO_2$ family. During charge, Li ions are constantly removed from the $LiMO_2$ structure, leading to the changes of lattice parameters. In general, the lattice parameter c expands first and then contracts, often to a value smaller than that of the pristine state at high voltage due to the nearly empty Li layer [159–161]; this may cause the structure collapse in c-axis direction leading to the irreversible damage of the structure and capacity fade. To solve this problem, studies were devoted to discover and design new materials aimed at reducing the c variation during cycling to achieve the high-capacity retention and long cycle life. The Li_2MoO_3 with the disordered α-$NaFeO_2$ structure has a reduced c variation range during cycling. In-situ XRD is employed to investigate how the structure changes during cycling [162]. Figure 7b displays the image plot of XRD spectra of a Li_2MoO_3 cathode during the first charge. The spectra of pristine and fully charged electrodes are in Figure 7a,c, respectively, and charge curve in Figure 7d, as well as lattice parameters obtained by Le Bail fitting of every spectrum with an $R\bar{3}m$ space group in Figure 7e. With careful examination of the evolution of the XRD image plot and the charge curve, the phase transformation can be summarized as follows:

(1) $1.5 < Li^+ < 2$ ($3 < V < 3.6$ V), (003) and (110) diffractions shift to the lower angles continuously, indicating a solid-solution reaction with increasing c and a lattice parameters of the phase I, but the percentage increase of a is greater than c, implying that Li ions are mainly removed from the $LiMo_2$ layers [163];
(2) $1.0 < Li^+ < 1.5$ ($3.6 < V < 3.7$ V), phase II, with the same layered structure as phase I, forms and grows at the expense of phase I. The lattice parameters of phase II are larger than those of phase I;
(3) $0.53 < Li^+ < 1.0$ ($3.7 < V < 4.8$ V), phase I is completely consumed and phase II grows via a solid solution route with a continuous increase of lattice parameters a and c.

Unlike the behavior of the cathode materials in the layered $LiMO_2$ family, the Li_2MoO_3 has a continuous increase of c until 4.8 V, suggesting no structure collapse in the c-axis direction during high voltage charge. During discharge, the phase transformation process is reversed, and the lattice parameters a and c decrease continuously, eventually to the values close to the pristine cathode. The stabilization of Li_2MoO_3 during cycling is mainly attributed to the migration of some Mo ions from $LiMo_2$ layer to the lithium layer, which is confirmed by STEM and neutron diffraction analysis of the pristine and fully charged Li_2MoO_3 [162,164]. Figure 7f,g display the STEM images obtained from $Li_{0.53}MoO_3$ and Li_2MoO_3 with the projection of Mo-O_6 octahedral along the *a*-axis. The images show that the Mo-O_6 octahedral changes from symmetric to distorted after de-lithiation and some Mo (black) move from the Li-Mo layer to the Li(white)-layer. The Mo ions in the Li^+ layer can strengthen the connection between the two transition metal layers and act as supports to prevent structure collapse in *c*-axis direction.

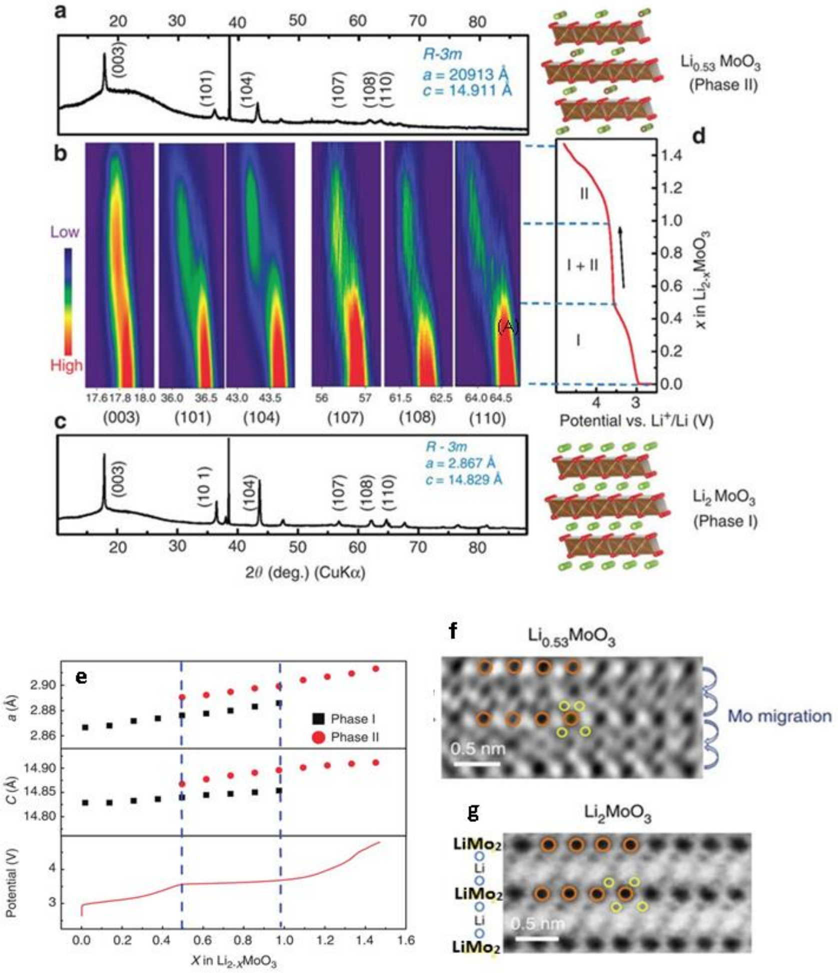

Figure 7. In-situ XRD of Li_2MoO_3 during the first charge. (**a**) The XRD pattern of the $Li_{2\text{-}x}MoO_3$ electrode right after charging to 4.8 V; the peak at 38.5° is from Al collector. (**b**) Contour plot of the evolution of (003), (101), (104), (107), (108) and (110) peaks during charge. (**c**) The XRD pattern of the Li_2MoO_3 electrode before charging; (**d**) Charge curve at a current density of 10 mA g^{-1} to 4.8 V. (**e**) Lattice parameter changes of Li_2MoO_3 during the first charge. (**f**,**g**) STEM lattice images of $Li_{2-x}MoO_3$ and Li_2MoO_3, respectively; where black: Mo, white: Li and yellow: O [162]; with permission from Springer Nature.

2. P2-$Na_{0.67}Ni_{0.33}Mn_{0.67}O_2$

Lu and Dahn [165] first showed that the Na^+ ions in the P2-$Na_{0.67}Ni_{0.33}Mn_{0.67}O_2$ structure can be completely extracted and the material has a capacity of ~170 mA g^{-1}. They investigated the crystal structure change during charge and discharge with in-situ XRD, and their galvanostatic cycling curve displays seven and five distinctive voltage steps during charge and discharge, respectively, which is comparable to the existence of nine steps and phases in the phase diagram of P2-Na_xCoO_2 [166]. The phase transformation identified during the cycling is between P2 and O2 structures [167]. Figure 8b is the XRD spectrum of pristine $Na_{0.67}Ni_{0.33}Mn_{0.67}O_2$; Figure 8a displays in-situ XRD spectra collected during charge between 2.5 and 4.4 V with applied current of 5 mA g^{-1}. During the initial stage of charge, the (00l) and (10l) peaks of P2-$Na_{0.67}Ni_{0.33}Mn_{0.67}O_2$ shift to a lower angle, while the (110) and (112) peaks shift to a higher angle indicating the expansion of the *c* axis and the contraction of the *a* axis. The in-situ XRD results indicate the crystalline phase is in P2 structure up to ~3.8 V, which is confirmed by electrochemical data and theoretical calculation. When the Na content is ~0.33 (~4 V), the broadening of the (10l) peaks is an indication of O2 type stacking faults in the P2 structure. A new set of Bragg peaks forms and grows on the 4.2 V plateau, accompanied by the gradual disappearance of the original peaks, suggesting a two-phase region. The new phase is determined to have an O2 structure. As the potential reaches 4.4 V, only the new phase is detected. During discharge (Figure 8d), the process is reversed; Na-ions are inserted back into the structure during discharge, and the structure transforms to P2 type, (Figure 8c). One of the advantages of the P2 phase is its stability in air and moisture, but the P2–O2 transformation involves a large volume change leading to fast discharge capacity fade.

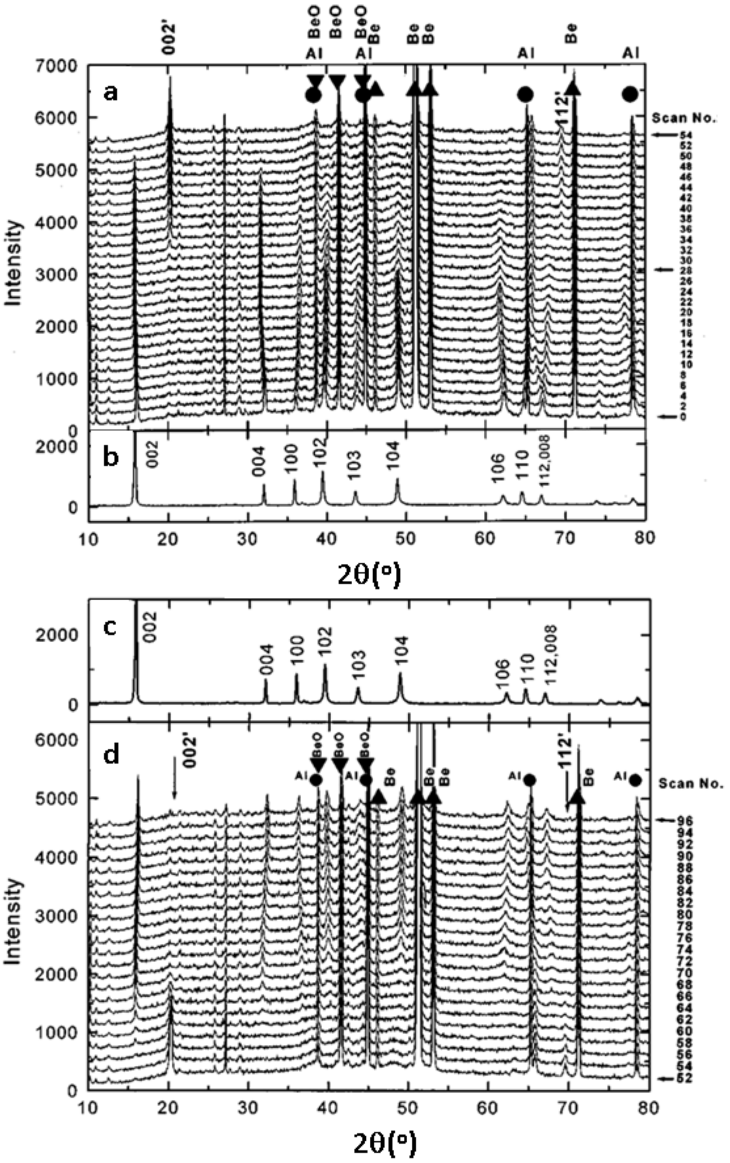

Figure 8. XRD pattern of P2-$Na_{2/3}Ni_{1/3}Mn_{2/3}O_2$ cell: (**a**) during first charge; (**b**) before cycling; (**c**) after first discharge; (**d**) during first discharge; Al, Be, BeO are contributions from cell components [167]; with permission from JES.

3. Doped P2-$Na_x[NiMn]O_2$

Many studies have focused on solving this phase instability problem caused by phase transformation. The inactive elements, such as Li^+, Mg^{2+} and Ti^{4+} are doped in the transition metal layer to stabilize the P2 structure during cycling, which improves the capacity and lengthen cycle life [168–170]. Xu et al. [170] investigated the Li substitution of transition metal in P2-$Na_{0.8}[Ni_{0.22}Mn_{0.78}]O_2$ with in-situ XRD. Figure 9a displays the evolution of XRD spectra of the $Na_{0.8}[Ni_{0.22}Li_{0.12}\ Mn_{0.66}]O_2$ cathode and a smooth charge curve to 4.4 V. Comparing these in-situ spectra to the spectrum of pristine powder (bottom, all the peaks are indexed by S.G. P63/mmc), the peaks shift from the original positions during Na-ion extraction, and all of the main peaks belong to the P2 phase. No new main peak is detected, indicating no significant phase transformation occurred, and the phase change is reversed during discharge from 4.4 to 2 V. Both the XRD spectra and the smooth charge curve suggest the de-intercalation follows the solid-solution route. Figure 9b plots the refined lattice parameters. Lattice parameter c increases continuously from beginning of charge ($Na^+ = 0.8$) to ~0.27 mole of Na^+ ions are extracted, which agrees well to the (004) peak shift to the lower 2θ direction in the range of $0.53 < Na^+ < 0.80$. Further extraction of Na^+ to Na^+ ~0.36 produces a slight shift of the position of the (004) line, corresponding to a small decrease of the c lattice parameter. The (100) peak shifts to the high 2θ direction during charge, resulting in a continuous decrease of lattice parameter a, which corresponds to the shortening of the distance between transition metals. The removal of Na^+ ions not only changes the lattice parameters, but also induces stacking faults which broaden the (10l) peaks in the XRD pattern [167,171]. The simulated XRD spectra with different percentage of stacking fault are shown in Figure 9c, and the width of the (10l) peaks increasedwith the increased amount of the stacking faults. The stacking faults prevents the P2–O2 phase transformation during the extraction of Na^+ upto 4.4 V, and the phase still maintains the P2 structure with local O2 type stacking fault. The strain and interface energies related to two phase separation are reduced by introducing the stacking fault in the structure, which stabilizes the P2 phase and increases capacity retention. When all of the Na^+ ions are extracted from the structure, the O2 phase is observed, which points out that Li^+ substitution can only postpone the P2–O2 phase transition to a higher voltage, bu cannot prevent the transformation to O2-type completely.

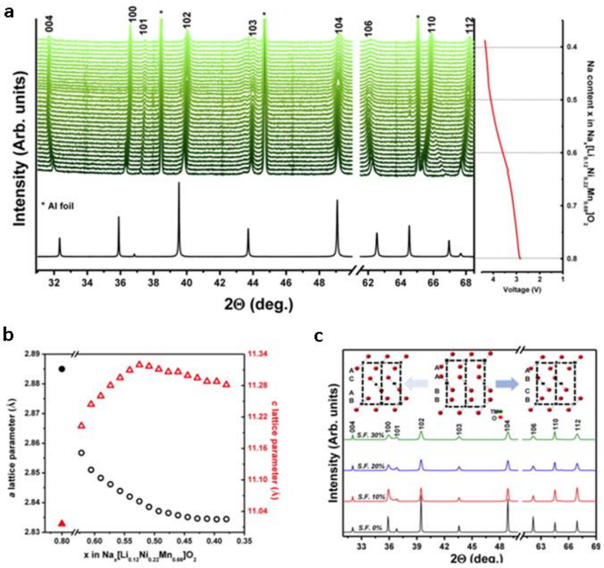

Figure 9. (**a**) In-situ XRD on $Na_{0.80}[Li_{0.12}Ni_{0.22}Mn_{0.66}]O_2$ during the first charge (Al collector is labelled as "*") and the corresponding charge curve. (**b**) Evolution of the a and c lattice parameters during the first charge obtained from Rietveld refinement (solid symbols represent a and c values in the pristine state). (**c**) XRD patterns obtained by simulating different amounts of O2-type stacking fault in P2 structure [170]; with permission from ACS.

Similar results were obtained with Mg-doped P2−$Na_{0.67}[Ni_{0.2}Mg_{0.1}Mn_{0.7}]O_2$ [168,172]. Figure 10a shows the charge-discharge curve of the cell cycled between 2 and 4.5 V and the corresponding XRD in Figure 10b. The evolution of the XRD spectra shows no characteristic peak of the O2 phase in the voltage range of 4.2–4.5 V. Instead, a broad peak as a shoulder on the (004) diffraction of P2 phase is observed at Na^+ ~0.35, which is a characteristic of the OP4 phase defined as an intergrowth structure between the P2 and O2-type structures [173]. As in the case of Li doping, the appearance of the OP4 phase stabilizes the P2 phase up to 4.5 V, which leads to improved cell performance.

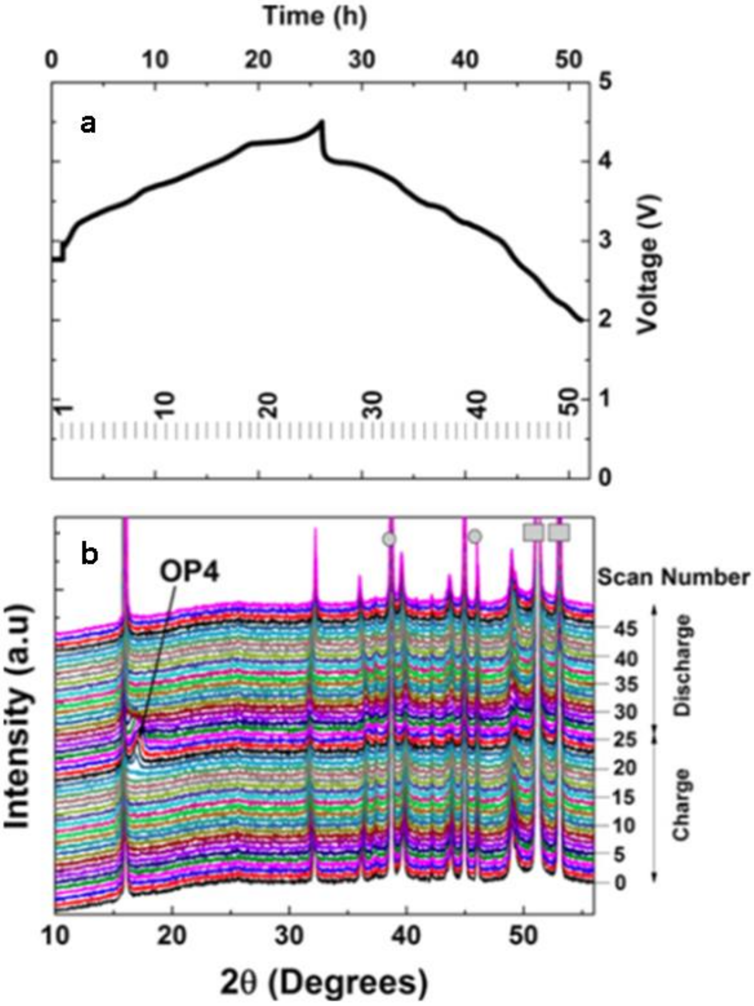

Figure 10. (**a**) Galvanostatic first charge-discharge curves. (**b**) In-situ X-ray diffraction of $Na_{0.67}Ni_{0.2}Mg_{0.1}Mn_{0.7}O_2$ showing the reversible evolution of P2 to OP4 phase transition at the end of charge and beginning of discharge. ■: Be window; ●:Al current collector [172]; with permission from ACS.

4. Graphite

Graphite is the most widely used anode material, and is capable of hosting many types of guest species, as well as simultaneously intercalating more than one different guest species. Graphite intercalation compounds (GICs) exhibit distinctive properties compared to pristine graphite.

- Graphite Anode in Lithium Ion Battery

He et al. studied the dynamic structural change of graphite during the electrochemical lithium intercalation at 1/3 C by in-situ high-energy synchrotron XRD [119]. Figure 11a displays a contour plot of XRD patterns and discharge curve for the Li/graphite cell from 1.53 to 0.001 V at a rate of

1/3 C. Figure 11b is the corresponding XRD spectra collected at different lithium values (x). During lithiation, the graphite (002) peak shifts and splits. At the beginning, the (002) peak shifts from 1.83 to 1.76° in the range of $0 < x < 0.3$, as well as increases in peak intensity. Between $0.3 < x < 0.5$, the (002) peak intensity increases with no obvious peak shift. When $x > 0.5$, a new peak forms at 1.69° and grows at the expense of the 1.76° peak. The 1.76° peak finally disappears, accompanied by the appearance of a series of continuous intermediate peaks between 1.69 and 1.76°. The presence of the two-phase region in graphite and the continuous intermediate diffraction peaks is not compatible with the classical stage mechanism. Based on the analysis of XRD spectra, the authors proposed a different mechanism to describe the dynamic lithium intercalation under high current. At the very beginning of lithiation ($x < 0.08$), Li^+ ions are randomly inserted into the graphite; as the process proceeds to $x \sim 0.3$, the intercalated lithium ions are distributed uniformly in the graphite. The structure transforms from AB lattice to the AA lattice with continued Li^+ ion insertion [174]. When $x > 0.5$, the outer layers of graphite are occupied first, resulting in a Li-rich region and generates a Li^+ gradient toward the inner layers of graphite. The growth of Li-rich phase as the continuous insertion of Li^+-ions leads to the full-lithiated phase, LiC_6.

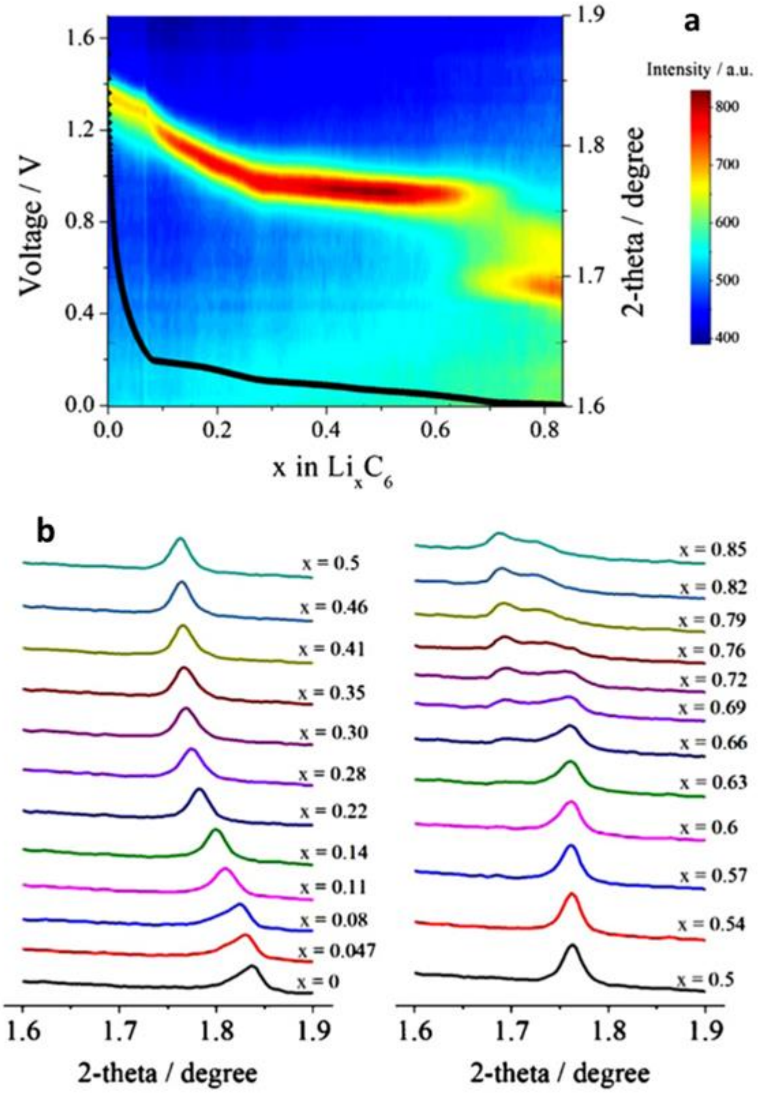

Figure 11. (**a**) Contour plot of XRD patterns and discharge curve from the Li/graphite cell discharged from 1.53 to 0.001 V at 1/3 C. (**b**) XRD patterns at 2θ between 1.6 and 1.9° showing the shift and split of graphite (002) peak as a function of *x* in Li_xC_6 [119], with permission from Elsevier.

- Graphite Anode in Sodium-ion Battery

Operando synchrotron XRD patterns were collected from a graphite anode in a Na half-cell with 1 M $NaPF_6$ in DEGDME (diethylene glycol dimethyl ether) cycled at a current density of 20 mA g^{-1}, see Figure 12 [95]. During sodium intercalation (sodiation) and de-intercalation (de-sodiation), the pristine graphite transforms into multiple new phases involving one or two-phase reactions and is completely restored to the pristine state after de-sodiation. The evolution of the XRD spectra implies a staging behavior during cycling. Initially, the (002) peak at ~27° down shifts slightly signifying a solid-solution reaction. The reaction proceeds until the graphite capacity reaches 31 mAh g^{-1} (t = 1.5 h, Na:C = 1:72), stage 3 GIC forms, and the (002) splits to (005) and (006). Moreover, with sodiation to Na:C = 1:50 (t = 2.2 h), a two-phase reaction started in this region, and stage 2 GIC forms at the expense of stage 3 GIC. After stage 3 GIC is exhausted, stage 1 GIC appears and grows at the expense of stage 2 GIC. The single phase of stage 1 GIC is observed after 4 h of sodiation, and exists in the range of Na:C from 1:28 to 1:21. Approaching the end of sodiation, new peaks appear between 12–14°, which are attributed to the in-plane super-structural ordering of the [Na-DEGME] complex. Correlating the results of operando XRD collected from electrochemical cycling and direct visualization coupled with density functional theory calculations, the authors proposed that Na intercalation occurs through multiple staging reactions; the final stage 1 GIC exists in the range of $1/28 < Na/C < 1/21$. In addition, the intercalated Na^+ ions and ether solvents are in the form of $[Na\text{-ether}]^+$ complexes, that are double stacked in parallel with graphene layers in the graphite. The association between the solvent and intercalated metal species suggests the possible tunability of Na storage properties.

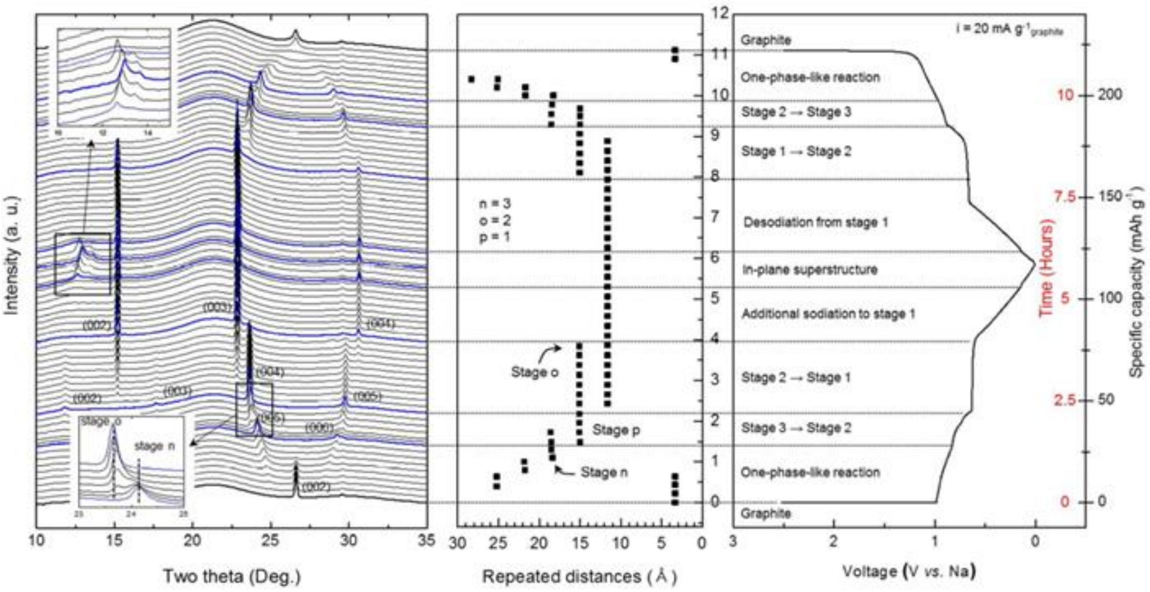

Figure 12. Operando synchrotron X-ray diffraction analysis of the structural evolution of the ternary Na-ether-graphite system observed during electrochemical solvated-Na-ion intercalation and de-intercalation of graphite in Na ∣ 1 M $NaPF_6$ in a DEGDME ∣ graphite cell [95]; with permission from RSC Publishing.

3.1.3. Spinel-$Li_4Ti_5O_{12}$

1. Spinel-$Li_4Ti_5O_{12}$ as anode in Li ion Battery

The spinel-$Li_4Ti_5O_{12}$ (LTO) is known as a "zero-strain" anode for lithium ion batteries. The phase transformation of LTO in the lithium ion battery is proposed as [175]:

$$Li_{3\,(8a)}\,[LiTi_5{}^{4+}]_{(16d)}O_{12(32e)} + 3e^- + 3Li^+ \leftrightarrow Li_{6(16c)}[LiTi_3{}^{3+}Ti_2{}^{4+}]_{(16d)}O_{12\,(32e)} \quad (1)$$

in the 2.5 to 1.0 V range. The pristine and discharged phases are $Li_4Ti_5O_{12}$ and $Li_7Ti_5O_{12}$, respectively. Both compounds belong to the $Fd\overline{3}m$ space group, and the insertion of three Li^+ ions in $Li_4Ti_5O_{12}$ results in little changes in the lattice parameters, thus it is classified as zero-strain. Studies were conducted on this material in the voltage range of 1.0 to ~0 V for the purpose of raising its capacity beyond 175 mAh g^{-1} [176–178]. The reaction mechanism during cycling, especially at low voltage was investigated by operando XRD [115,175]. Figure 13 [115] presents the development of three characteristic diffraction lines and the corresponding image plots of $Li_4Ti_5O_{12}$ cycled between 3.0 and 0.0 V. The (111), (311) and (400) peaks do not shift during discharge from 3.0 to 1.0 V, but with further discharge to 0.0 V, all three peaks shift to low angles gradually; they move reversibly to their initial positions upon charge to 1.0 V. This peak shift at low voltage is attributed to the two more Li ions inserted to the 8a sites of $Li_7Ti_5O_{12}$ [175]:

$$Li_{6(16c)}[LiTi_3{}^{3+}Ti_2{}^{4+}]_{(16d)}O_{12(32e)} + 2e^- + 2Li^+ \leftrightarrow Li_{2(8a)}Li_{6(16c)}\ [LiTi_5{}^{3+}]_{(16d)}O_{12(32e)} \quad (2)$$

The continuous shift of the diffraction lines suggests this phase transition follows a solid-solution path. The authors also calculated the lattice parameters of the fully discharged anode, which are very close to those of the original LTO with only 0.38% volume change. The small volume expansion indicates that the "zero strain" property is kept even at low voltage ~0.0 V.

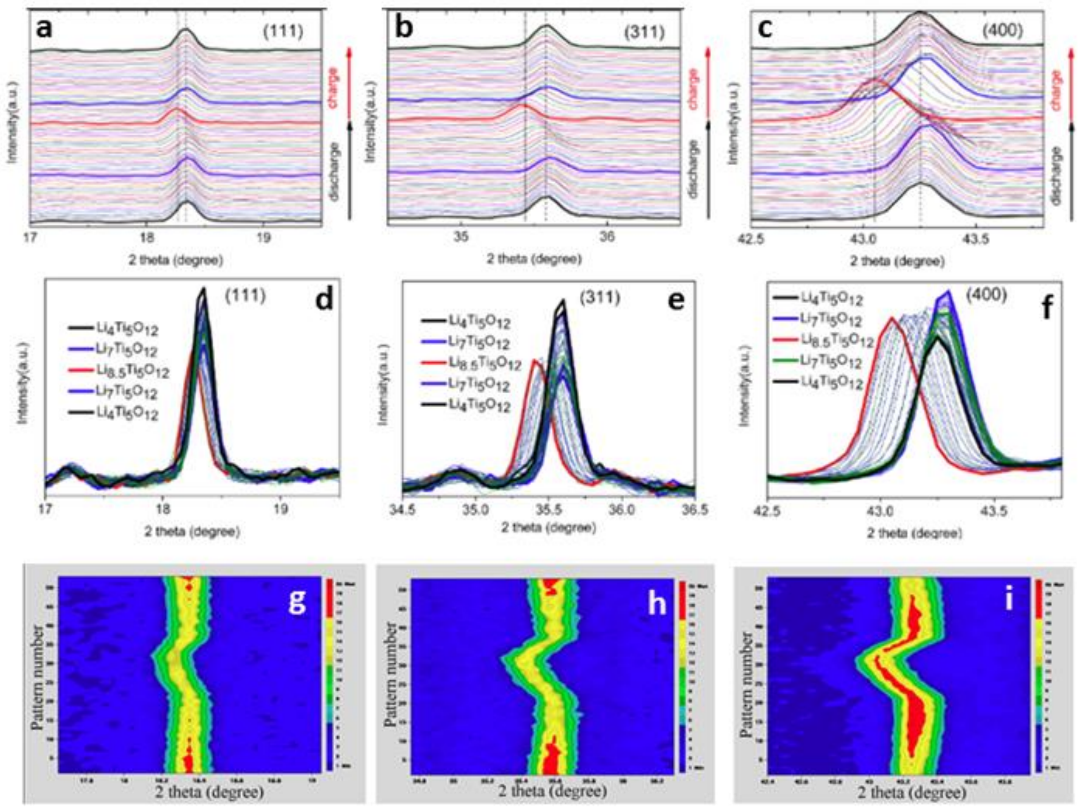

Figure 13. (**a**–**c**) Evolution of (111), (311) and (400) diffractions of $Li_4Ti_5O_{12}$ during the first discharge/charge between 3.0 and 0 V and their image plots (**g**–**i**). (**d**–**f**) Highlighted spectra with corresponding compositions [115]; with permission from ACS.

1. Spinel-$Li_4Ti_5O_{12}$ as anode in Na ion Battery

The $Li_4Ti_5O_{12}$ can also be used as an anode in a sodium ion battery, despite the large volume change involved due to bigger size of Na^+ than Li^+ [179,180]. The mechanism of sodium insertion and extraction is different from that of lithium, and was studied by various techniques, including X-ray diffraction, electron microscopy, X-ray absorption, etc [60,99,181,182]. Figure 14a illustrates the evolution of the synchrotron XRD spectra during discharge-charge collected from a cell with C-$Na_3V_2(PO_4)_3$ cathode and $Li_4Ti_5O_{12}$ anode in the range of 0.5–3.0 V at C/10 rate. The $Li_4Ti_5O_{12}/Li_7Ti_5O_{12}$ peaks shift slightly to the lower two theta direction during cycling, suggesting a solid-solution reaction. On the other hand, a new set of peaks attributed to $Na_6LiTi_5O_{12}$ appears as discharge approaches the end and reaches maximum during the following charge process, then disappears before the end of charge. This delayed phase appearance is a result of slow Na^+ diffusion in the crystal structure. The formation of $Na_6LiTi_5O_{12}$ indicates that phase separation dominates the reaction. Equation (3) describes a three-phase separation mechanism for the sodium insertion/extraction in/out of LTO that was verified via STEM with the observation of the co-existence of three phases in a semi-discharged electrode as shown in Figure 14b [60].

$$2[Li_3]_{8a}V_{16c}[LiTi_5]_{16d}O_{12} + 6Na^+ + 6e^- \leftrightarrow V_{8a}[Li_6]_{16c}[LiTi_5]_{16d}O_{12} + V_{8a}[Na_6]_{16c}[LiTi_5]_{16d}O_{12} \quad (3)$$

where V = vacancy.

In addition, the influence of LTO particle size on the phase transformation of a chemical sodiated $Li_4Ti_5O_{12}$ was investigated by operando synchrotron XRD [99]. A solid-solution reaction was observed over a wide range during Na insertion in the nanosized LTO (~44 nm), which is similar to the case of LFP.

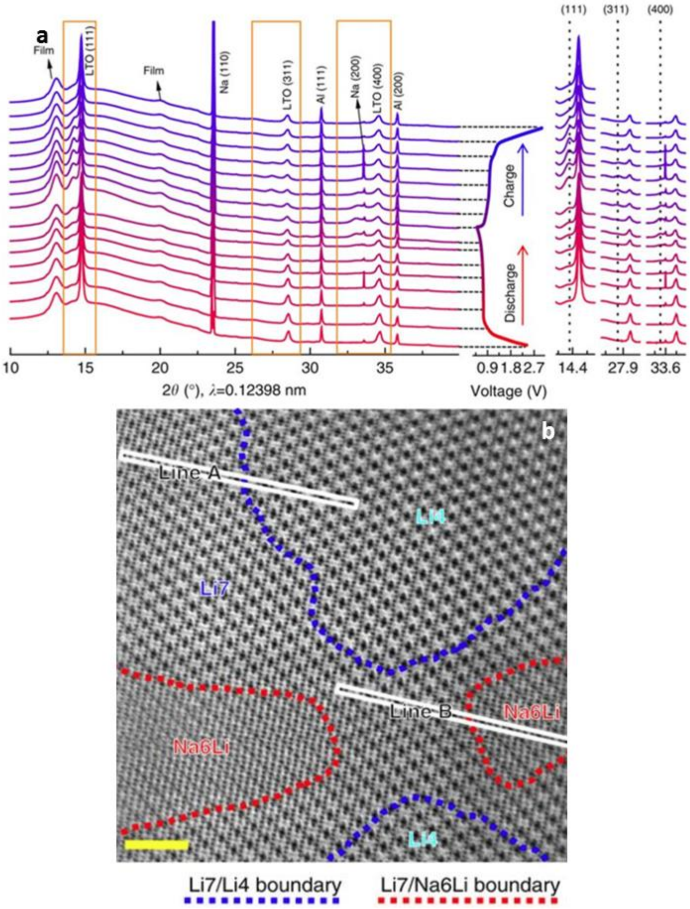

Figure 14. (**a**) In-situ synchrotron XRD patterns of the $Li_4Ti_5O_{12}$ electrode in a sodium-ion battery collected during the first cycle. For the $Li_4Ti_5O_{12}/Li_7Ti_5O_{12}$ phases, the main peaks correspond to (111), (311) and (400) reflections, highlighted at the right and peaks of the $Na_6LiTi_5O_{12}$ phase are marked by black dotted lines. (**b**) An annular-bright-field STEM image showing a three-phase area from a partially electrochemically sodiated $Li_4Ti_5O_{12}$ nano-particle, Scale bar, 2 nm [60]; with permission from Springer Nature.

3.1.4. Electrodes for Aqueous Battery

The aqueous lithium/sodium-ion batteries are low cost and safe choices for large-scale applications due to the use of low cost, non-flammable and highly conductive aqueous electrolyte, as well as being environmental benign. Some electrode materials have been proposed and evaluated [183–185], but the practical application of the aqueous batteries still faces great challenges. Recently, more and more investigations were dedicated to understand the working and degradation mechanisms of electrodes for aqueous batteries in order to enhance the battery performances.

1. Tunnel-type Ti-$Na_{0.44}MnO_2$

Wang et al. [186] investigated Ti-substituted $Na_{0.44}MnO_2$ oxide as a negative electrode for aqueous Na^+-ion batteries and found it possesses superior cyclability. $Na_{0.44}MnO_2$ has an orthorhombic lattice with S.G. of Pbam; its structure has a large "S" typed tunnel. There are five different crystallographic sites for Mn ions, labelled as Mn(1) to Mn(5) and three sites for Na ions; the double and triple rutile-type chains of edge-sharing MnO_6 octahedral and single chains of corner-sharing MnO_5 support the structure and make it stable during Na^+ extraction and insertion, see Figure 15d. Operando XRD and spherical aberration-corrected STEM are utilized to probe the sodium storage mechanism and accurately identify the Ti substitution sites. Figure 15a–c show the structure evolution of $Na_{0.44}[Mn_{0.44}Ti_{0.56}]O_2$ during a cycle of Na extraction and insertion, as well as the corresponding variations in lattice parameters. The main XRD reflections, such as (040), (130), (140), show a continuous peak shift during Na insertion/extraction and no new phase is detected in most part of the process. Therefore, the main crystal structure is maintained and the phase transition mainly follows a solid-solution path, whereas the un-doped $Na_{0.44}MnO_2$ manifests a two-phase reaction behavior [187]. In addition, a small biphasic region can be observed at the end of discharge, which the authors attribute to the smaller unit cell volume of $Na_{0.44}[Mn_{0.44}Ti_{0.56}]O_2$ than $Na_{0.66}[Mn_{0.44}Ti_{0.56}]O_2$ as well as the slow kinetics of the phase transformation. To understand the effect of Ti on the electrochemical performance and reaction mechanism, the crystal structure of $Na_{0.44}[Mn_{0.44}Ti_{0.56}]O_2$ and the valences of the Ti and Mn cations were studied by STEM/EELS and in-situ XAS. Figure 15e,f present the high-angle annular dark-field STEM (HAADF-STEM) and EELS images of as-made $Na_{0.44}[Mn_{0.44}Ti_{0.56}]O_2$ along the [001] zone axis. The EELS image clearly shows that Ti^{4+} replaces Mn^{4+} on the Mn(1)-Mn(4) positions, but not on Mn(5), which agrees with their Rietveld refinement of the synchrotron XRD spectra and the stable structure configuration from their density function calculation. During cycling, Ti and Mn(5) are at constant valence of 4^+, whereas Mn(2) and Mn(3) participate in the redox reaction. This anode material has very stable cycling performance, which demonstrates the role of Ti in stabilizing the $Na_{0.44}MnO_2$ structure. This study reveals the difference in working mechanisms of this Ti-doped and un-doped tunnel-type electrode material and is helpful for designing new materials for high-performance aqueous sodium rechargeable batteries.

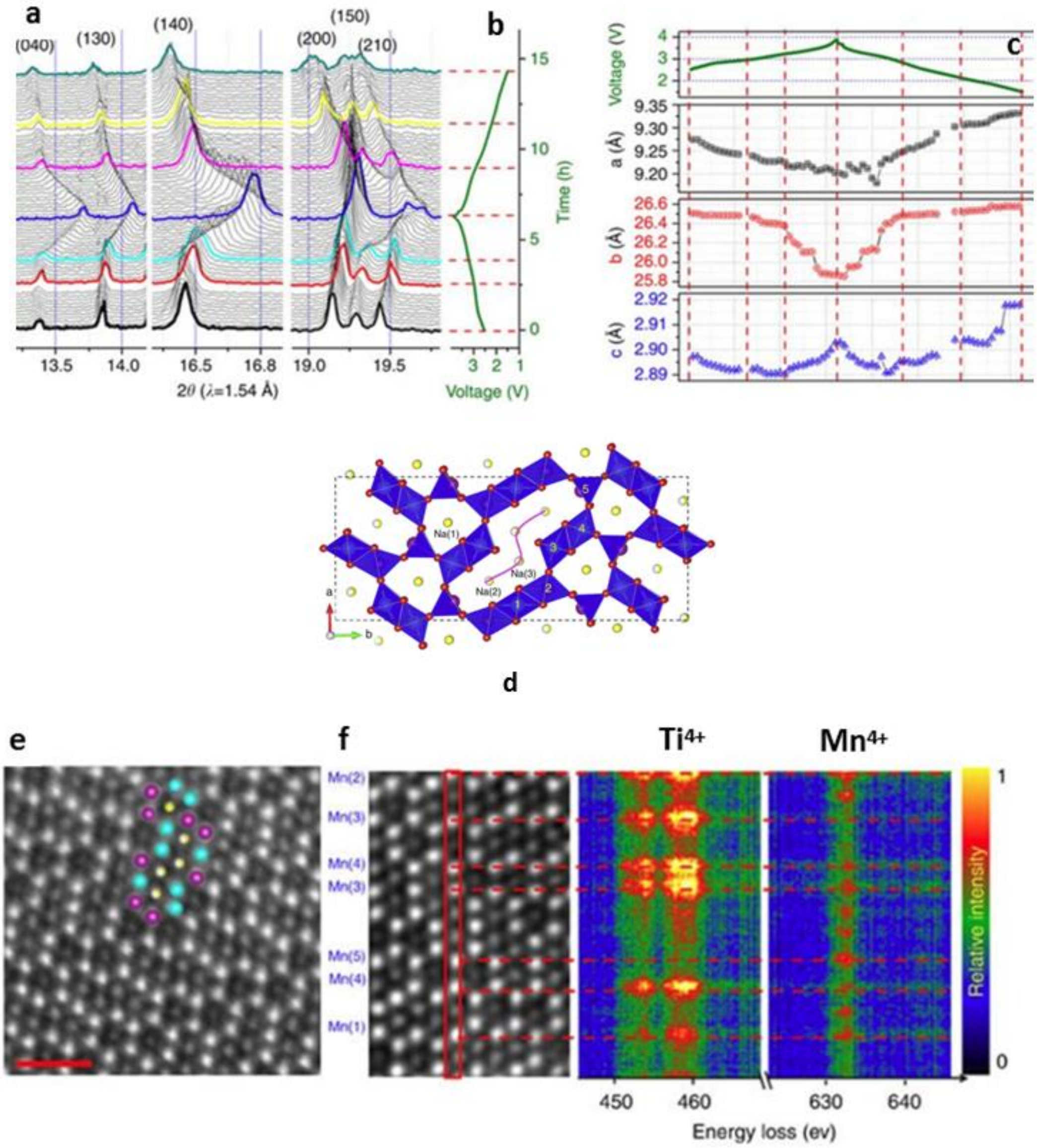

Figure 15. (**a**) Operando XRD patterns collected during the first charge-discharge of a Na/$Na_{0.44}[Mn_{0.44}Ti_{0.56}]O_2$ cell at C/10 rate between 1.5 and 3.9 V. (**b**) Charge-discharge curve. (**c**) Lattice parameter variations correspond to (**a**). (**d**) General structure view along *c*-axis showing five crystallographic sites for manganese and three sites for sodium. (**e**) HAADF-STEM image for as-prepared $Na_{0.44}[Mn_{0.44}Ti_{0.56}]O_2$ along [001] zone axis. (**f**) The EELS image of $Na_{0.44}[Mn_{0.44}Ti_{0.56}]O_2$. Scale bar, 1 nm, [186]; with permission from Springer Nature.

1. $LiMn_2O_4$-$FePO_4$ aqueous Battery

For lithium-ion aqueous batteries, the main difficulty lies in capacity fade of the anode materials, such as activated carbon, LiV_3O_8, V_2O_5, $LiTi_2(PO_4)_3$, TiO_2 and $Li_4Ti_5O_{12}$ [188–192]. Olivine-structured $FePO_4$ and amorphous $FePO_4{\cdot}2H_2O$ were explored as anodes for aqueous lithium-ion batteries. Figure 16 plots the development of the XRD spectra of a $LiMn_2O_4$-$FePO_4$ aqueous battery during charge-discharge. Olivine $FePO_4$ undergoes a reversible two-phase transformation (FP ↔ LFP), similar to that in organic electrolytes, confirming the lithium intercalation and de-intercalation processes. Simultaneously, the $LiMn_2O_4$ cathode shows continuous reversible shifts of all the peaks indicating a solid-solution reaction. On the other hand, the in situ XRD spectra of amorphous anode in the $LiMn_2O_4$-$FePO_4$ $2H_2O$ cell show the start of crystallization and nano-crystals are observed by

TEM. Comparing the two materials, olivine $FePO_4$ delivers higher capacity and higher rate, whereas amorphous $FePO_4{\cdot}2H_2O$ has a longer cycle life at a slower rate [193].

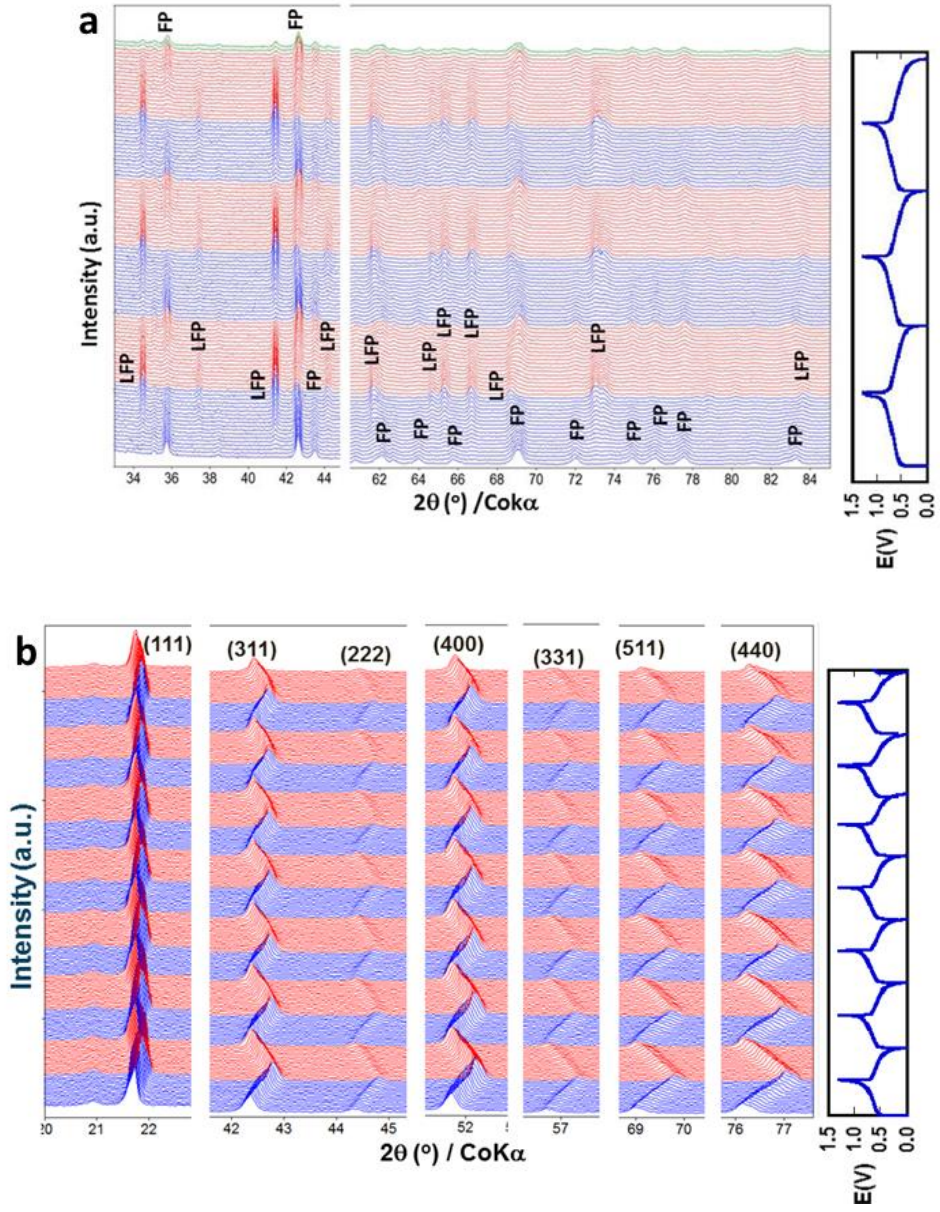

Figure 16. Evolution of XRD patterns of (**a**) olivine $FePO_4$ and (**b**) $LiMn_2O_4$ upon cycling [194], with permission from ACS.

3.2. Degradation Mechanisms

One of the challenges that rechargeable batteries face is electrode degradation, which reduces battery capacity and shortens battery life. Understanding the degradation mechanism is the first step to solve the problem. Liu et al. [122] used the in-situ synchrotron XRD with a commercial 18650 LFP cell at different cycles to investigate the structure changes in the course of long term cycling to elucidate the capacity fade mechanism. Figure 17 plots the evolution of XRD spectra of the first and 2500th cycles during discharge at 1C rate. As the depth of discharge increases, the lithium ions are extracted from lithiated graphite and inserted into FP to form LFP. At the end of first discharge, all FP peaks disappear, see Figure 17a, whereas the FP peaks are still observed at the end of the 2500th discharge, Figure 17b.

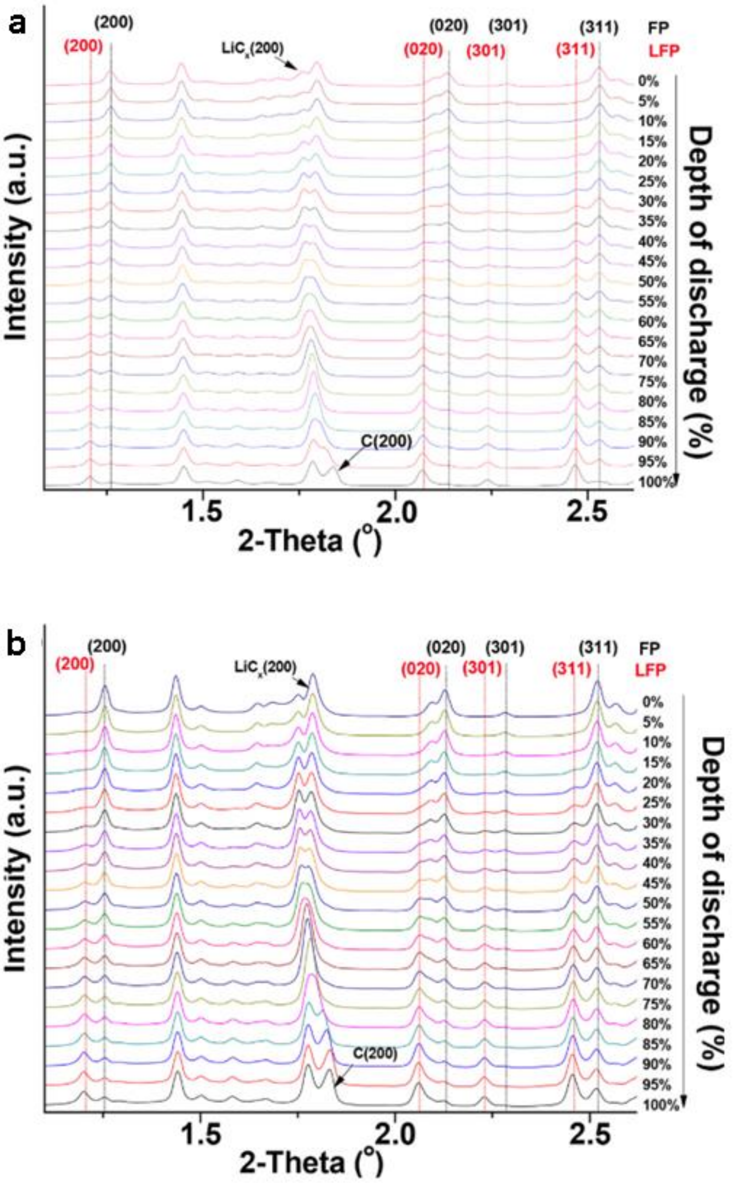

Figure 17. XRD patterns between 2θ = 1.0 and 2.8° from discharge at 1C rate as a function of DOD during the (**a**) 1st and (**b**) 2500th cycles [122]; with permission from ACS.

The authors suggest that the presence of the FP phase is an indication of insufficient active lithium to complete the FP to LFP transformation at the end of discharge, and conclude that the loss of the source of active lithium-ion is the primary cause of the capacity fade. The amount of the inactive FP at 100% depth-of-discharge is proportional to the decrease of the available lithium-ion during cycling. As the numbers of cycle increase, the solid-solution range near the stoichiometry FP decreases, and the FP-LFP transition is close to the two-phase reaction. The decay of the solid-solution behavior is associated with the degradation of the rate performance of LFP at higher cycles.

3.3. Thermal Stability

The operando XRD is a technique that can be used in many aspects to study the performances of rechargeable batteries. Several examples presented above concern the working and degradation mechanisms of various electrode materials in non-aqueous and aqueous electrolytes. In addition, this technique is also useful in the investigation of the thermal stability of electrodes, which is an important issue in battery application.

1. O3-type $NaNi_{2/3}Sb_{1/3}O_2$

The thermal stability of layered O3-type $NaNi_{2/3}Sb_{1/3}O_2$ cathode material was studied by in-situ high temperature XRD (HTXRD). The $NaNi_{2/3}Sb_{1/3}O_2$, which was synthesized at 950 °C, has a rhombohedral lattice with S.G. of $R\bar{3}m$. It exhibits a reversible capacity of 52.5 mAh g^{-1} after 100 cycles with capacity retention of 62.4%. The operando XRD conducted during room temperature cycling reveals the reaction goes through a complicated multiphase phase transformation during charge, i.e., O3 → O3 + P3 → P3 → O1 + P3 → O1, the process is reversed upon discharge. The thermal stability test is conducted on $NaNi_{2/3}Sb_{1/3}O_2$ to elucidate the structural evolution during cycling and its behavior at high temperature. Figure 18 presents the XRD data from a charged $NaNi_{2/3}Sb_{1/3}O_2$ between 100 and 500 °C with 25 °C increment. The diffraction peaks show the co-existence of P3 (red) and O3 (black) phases with P3 dominant initially. As the temperature increases to 500 °C, only peak shifts due to cell expansion upon heating are observed. No new peak is detected, indicating the stabilities of P3 and O3 phases up to 500 °C, which demonstrates a superior thermal stability for sodium storage [194].

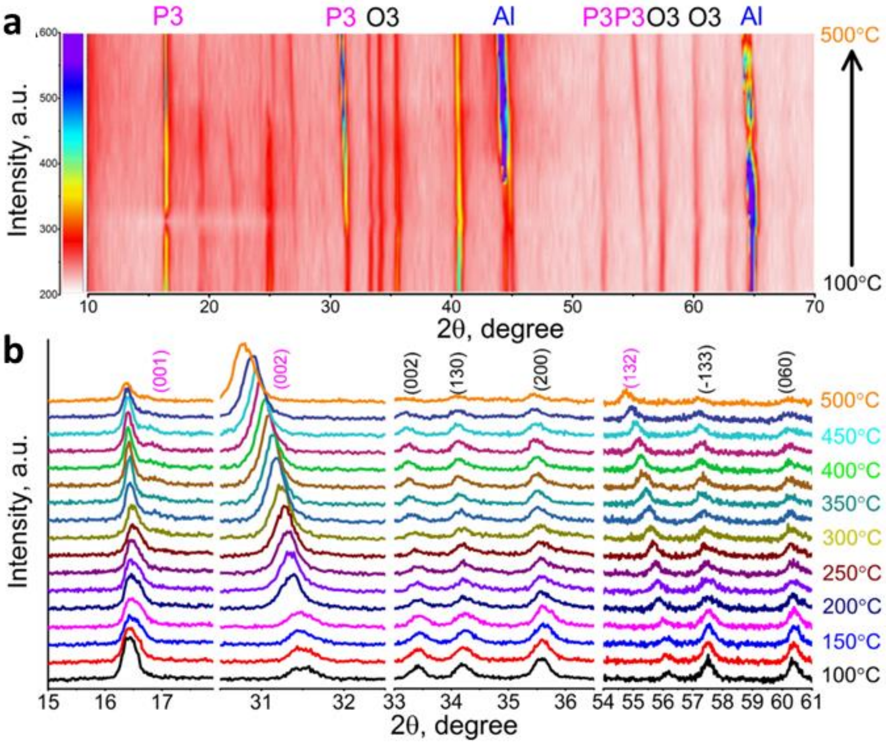

Figure 18. (**a**) Image plots of HTXRD spectra of charged $Na_xNi_{2/3}Sb_{1/3}O_2$ heated from 100 to 500 °C. (**b**) The corresponding selected diffraction patterns, peaks labelled pink is P3 phase, and black is O3 [194]; with permission from Elsevier.

2. Layered-$LiNi_xMn_yCo_zO_2$

The thermal stability of charged $LiNi_xMn_yCo_zO_2$, where x + y + z = 1, with different cation ratios are examined by operando HTXRD and operando mass spectroscopy (MS). The layered $LiNi_xMn_yCo_zO_2$ has rhombohedral lattice and belongs to $R\bar{3}m$ space group. Figure 19a–d present image plots of the developments of XRD patterns from a series of delithiated $LiNi_xMn_yCo_zO_2$ cathodes in the temperature range of 25–600 °C [93]. The images show that these charged materials undergo a specific path of phase transitions from layered to spinel, and then to rock-salt as the heating temperature increases; the results are summarized in Table 1.

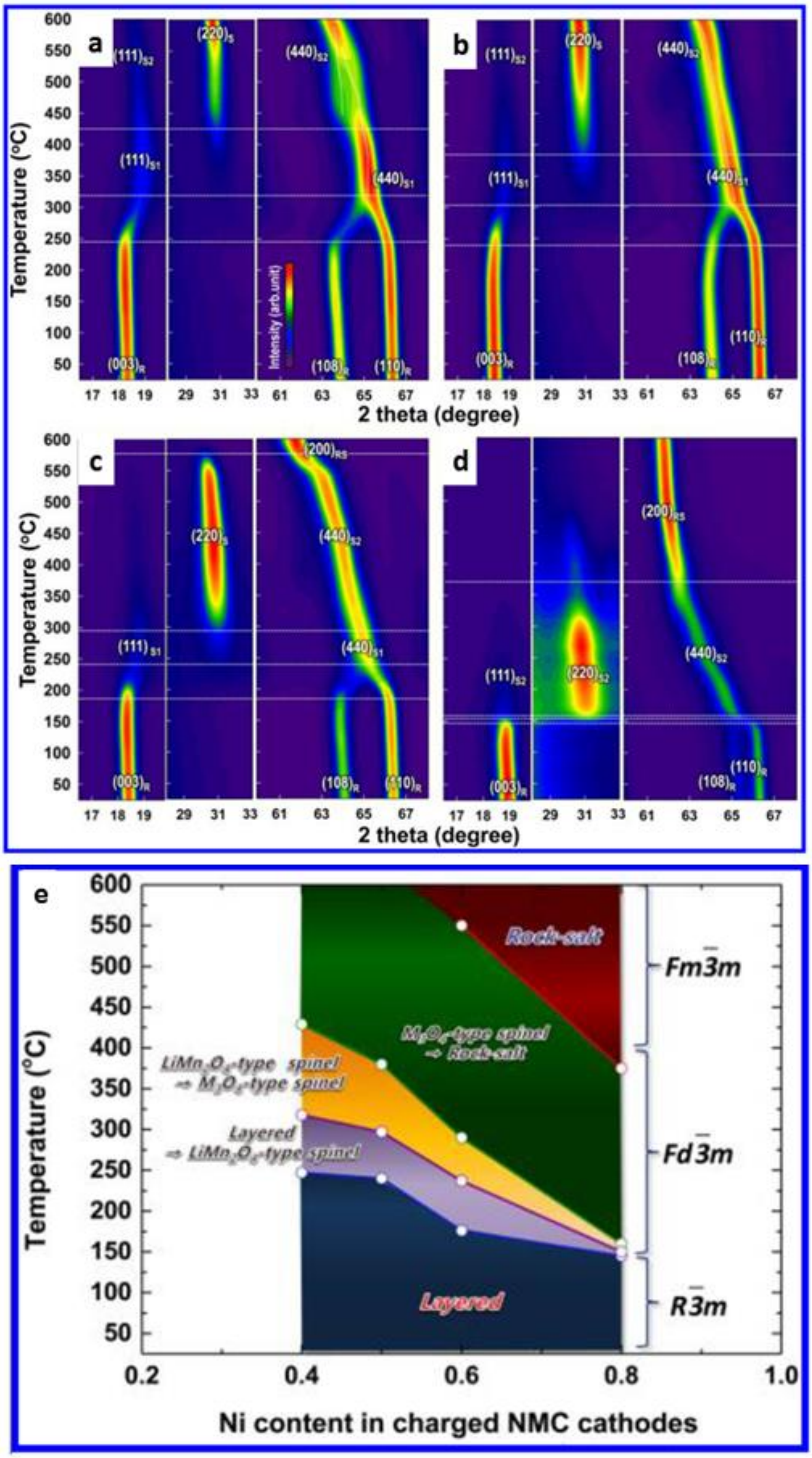

Figure 19. Image plots of XRD patterns at the selected 2θ range for the charged (**a**) NMC433, (**b**) NMC532, (**c**) NMC622 and (**d**) NMC811. (**e**) Schematic illustration depicting the phase stability map of the charged NMC cathode during heating [93]; with permission from ACS.

Table 1. Phase transformation temperatures obtained from operando HTXRD and the peak temperature of oxygen release from MS.

Pristine Cathode	**$LiNi_{0.4}Mn_{0.3}Co_{0.3}O_2$ (NMC433)**	**$LiNi_{0.5}Mn_{0.3}Co_{0.2}O_2$ (NMC532)**	**$LiNi_{0.6}Mn_{0.2}Co_{0.2}O_2$ (NMC622)**	**$LiNi_{0.8}Mn_{0.1}Co_{0.1}O_2$ (NMC811)**
After charge	Li = 0.34	Li = 0.29	Li = 0.27	Li = 0.22
Phase at 25 °C	R	R	R	R
T_0–T_f (°C) **NMC→S1**	245–325 ΔT = 80 °C	235–315 ΔT = 80 °C	185–245 ΔT = 60 °C	T_0 = 135
T_0/T_f (°C) **S1→S2**	T_0 = 450	T_0 = 400	T_0 = 310	T_f = 155
T_0/T_f (°C) **S2→RS**	no RS up to 600 °C	no RS up to 600 °C	T_0 = 550	T_f = 365
Phases at 600 ° C	S1 + S2	S2	RS	RS + Ni (minor)
$T_{peak, O2}$ (°C) **(from MS)**			~230	~150
Peak shape	Broad/low ~220–320 °C	Broad/low ~220–320 °C	Broad/medium ~170–340 °C	sharp/high ~130–260 °C

R: $Li_{\alpha}Ni_xMn_yCo_zO_2$ (x + y + z = 1), layered structure, S.G. = R$\bar{3}$m; S1:$LiNi_xMn_yCo_zO_4$ (x + y + z = 2), spinel structure, S.G. = Fd$\bar{3}$m; S2: $Li_{\alpha}Ni_xMn_yCo_zO_4$ (α + x + y + z) = 3, spinel structure, S.G. = Fd$\bar{3}$m; RS: $Li_{\alpha}Ni_xMn_yCo_zO$ (α + x + y + z = 1), rock salt structure, S.G. = Fm$\bar{3}$m; T_0 and T_f are the starting and ending temperatures for a phase transformation, respectively.

The results in Table 1 indicate that the thermal stability of the charged NMC is mainly governed by the nickel content; more nickel in the sample results in lower starting temperature for the phase transformation. This is due to the least stable nature of nickel among the three transition metals and the large amounts of unstable Ni^{4+} are reduced to Ni^{2+}, which is accompanied by the release of oxygen during phase transformation. In addition, Mn is the most thermally stable element enhancing the thermal stability. A sudden decrease in thermal stability is observed by changing the composition from NMC532 to NMC622, indicating that NMC532 is the optimal composition for balancing good thermal stability and reasonable high capacity. A diagram of phase stability vs. temperature and Ni content is constructed based on the results discussed above, which can act as a guide for the design of the cathode materials, Figure 19e [93].

3. $LiNi_{0.75}Co_{0.15}Al_{0.05}Mg_{0.05}O_2$ (NCA-Mg)-graphite cell

Overcharging lithium-ion batteries leads to rapid and exothermic reactions accompanied by side chemical reactions at the cathode and anode, which is a complex process and has direct impact on the cell life and safety. The behavior of a $LiNi_{0.75}Co_{0.15}Al_{0.05}Mg_{0.05}O_2$-graphite cell under overcharge condition at 30 and 50 °C was probed by in-situ synchrotron XRD and X-ray absorption fine structure spectroscopy (XAFS). Figure 20a,b display the (003) diffraction (2θ: 18–19°) of NCA-Mg (rhombohedral, R$\bar{3}$m) and (002) diffraction (2θ: 24–26.5°) of graphite (hexagonal, P63mc) at 30 and 50 °C with their voltage profiles in Figure 20c. The evolution of the diffractions can be divided into low, mid and high voltage regions. The following observations were noted during charge:

(1) Low voltage region ($0 \leq SOC \leq 100\%$, $V \leq 4.1V$). The peak $(003)_{NCA\text{-}Mg}$ shifts to lower diffraction angle owing to the expansion of distance between transition metal layers induced by lithium de-intercalation. This distance reaches maximum when the cells are charged at 100% SOC (C1 in Figure 20a,b) at both 30 and 50 °C, implying the side reactions at NCA-Mg electrodes are negligible in this region;

(2) Mid voltage region ($100\% < SOC < {\sim}200\%$, $V \leq 6.6$ V). The $(003)_{NCA\text{-}Mg}$ peaks shift back to higher angle caused by the contraction of the interlayer distance. The shift of $(003)_{NCA\text{-}Mg}$ is slower at 50 °C than at 30 °C in the region marked as OC2, suggesting more side reactions at 50 °C than at 30 °C. The X-ray absorption results indicate that the oxidation of nickel and cobalt in NCA-Mg reached the maximum values at cell voltage of 6.6 V;

(3) High voltage region (~200% < SOC, V > 6.6 V). The rate of $(003)_{\text{NCA-Mg}}$ peak shift slows down in the case of 30 °C, suggesting that side reactions accelerated at the NCA-Mg cathode in the high voltage region, labeled as OC1 in Figure 20a. The cell at 50 °C exhibits no $(003)_{\text{NCA-Mg}}$ peak shift in the overcharge region with voltage > 8 V (OC3), indicating that the charging current is fully consumed by side reactions at NCA-Mg positive-electrode. On the anode side, lithium ions intercalate into graphite during charge. At 30 °C, fully-intercalated graphite, LiC_6, is formed at the overcharge state, marked with "Li-GIC". Graphite cannot accommodate more Li^+ in the structure with charging the cell beyond this point, which results in lithium plating on the graphite anode [195,196]. In the cell at 50 °C, graphite is not fully intercalated with Li^+ even at 10 V owing to the increased side-reactions on the graphite at this temperature. Based on the operando XRD and SAFS results, the authors proposed different side reaction mechanisms for the overcharged cells at 30 and 50 °C, which can help researchers to understand the overcharge effect on both cathode and anode, and to design batteries that can reduce and optimize the side reactions for the long life and safe batteries [197].

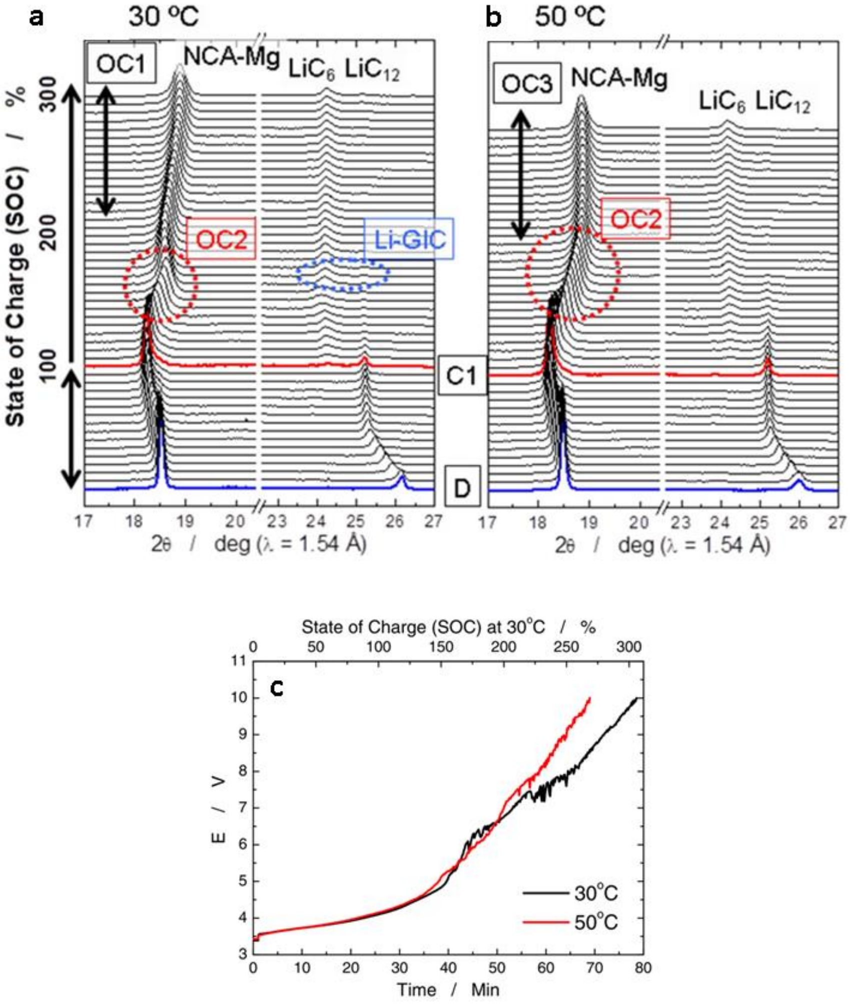

Figure 20. X-ray diffraction patterns for NCA-Mg and graphite during (over-)charging at (**a**) 30 and (**b**) 50 °C. The SOC at 0 and 100% of the lithium-ion cells are shown in blue and red, respectively. (**c**) Voltage profile of NCA/Mg-graphite cells cycled to 10 V at 2C-rate at 30 or 50 °C. The state of charge (SOC) at 100% is defined as 4.1 V terminal cell voltage, and the SOCs at 30 °C are displayed in the figure [197]; with permission of JES.

3.4. Heat Treatment

In-situ XRD is widely used in characterizing and monitoring phase formation, phase transformation, crystal growth, etc. during heat treatments. The observations provide valuable information on the optimization of the heat-treatment conditions for synthesizing materials with the desired structure and properties. Following are two examples of applying HTXRD in guiding the synthesis of suitable electrode materials.

3.4.1. Phase evolution of $LiFePO_4$ Precursor

Parallel in-situ HTXRD and HTTEM studies on the $LiFePO_4$ precursor made by a sol-gel method were conducted and revealed in-depth information on structure and morphology evolution of $LiFePO_4$ precursors during heat treatment at the centi-meter and nano-meter scales. The optimum heat-treatment parameters to produce the high-quality electrode materials were verified by the electrochemical performance of the materials heated at different temperatures.

Figure 21a,b show the evolution of XRD spectra with temperatures in inert atmosphere. The starting precursor is amorphous and the nucleation of $LiFePO_4$ starts at ~425–445 °C. The growth and sharpening of the diffraction peaks as the temperature increases is indicative of the crystal size increase. The average crystallite sizes, estimated by the Scherrer equation [198], changes from 14 to 79 nm with a temperature increase from 425 to 900 °C. The authors calculated the unit cell parameters of LFP as a function of temperature and derived a relation of volume thermal expansion with the temperature.

Figure 21c presents the in-situ HRTEM micrographs taken at different temperatures of a specific particle with corresponding selected area electron diffraction patterns (SAED) at the right. The crystalline lattice fringes are initially observed between 450 and 500 °C. At 450 °C, some particles show the lattice fringes, whereas others show small clusters of arranged atoms. The appearance of these clusters is an early indication of nucleation, which agrees with the in-situ XRD spectrum. The HRTEM images and SAED patterns indicate the formation and growth of $LiFePO_4$ crystallites occur between 500 and 700 °C. These images show that the morphology of the particles become more porous, meanwhile, their surfaces and shapes changed slightly with increasing temperature.

Of the LFP heated from 500–900 °C, the one heated at 800 °C has the best electrochemical performance, despite a capacity that is still much lower than the theoretical values. The combination of parallel in-situ XRD and in-situ TEM studies with electrochemical performances of the materials reveals (1) the optimum heating conditions for obtaining materials with high performance; (2) the temperature effects on phase evolution, crystallinity and morphology of $LiFePO_4$; and (3) the effect of crystal structure, crystal size and morphology on the electrochemical properties, which are essential information to produce high-quality electrode materials [199].

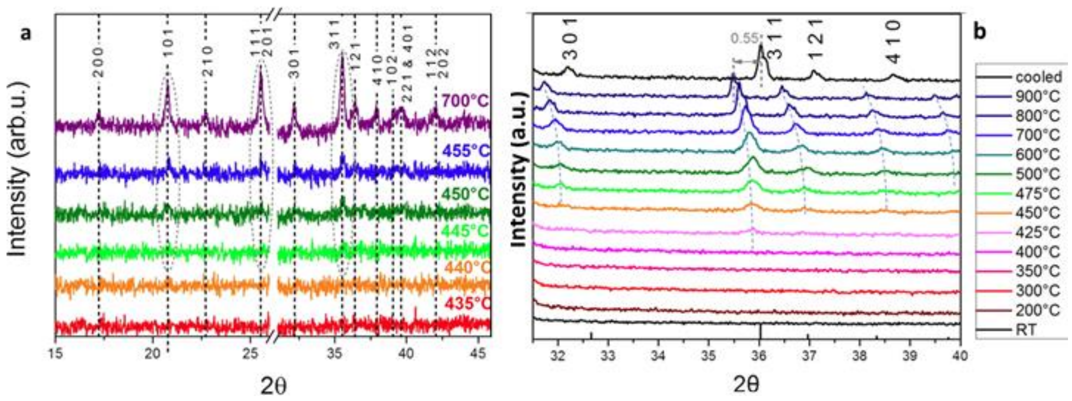

Figure 21. *Cont.*

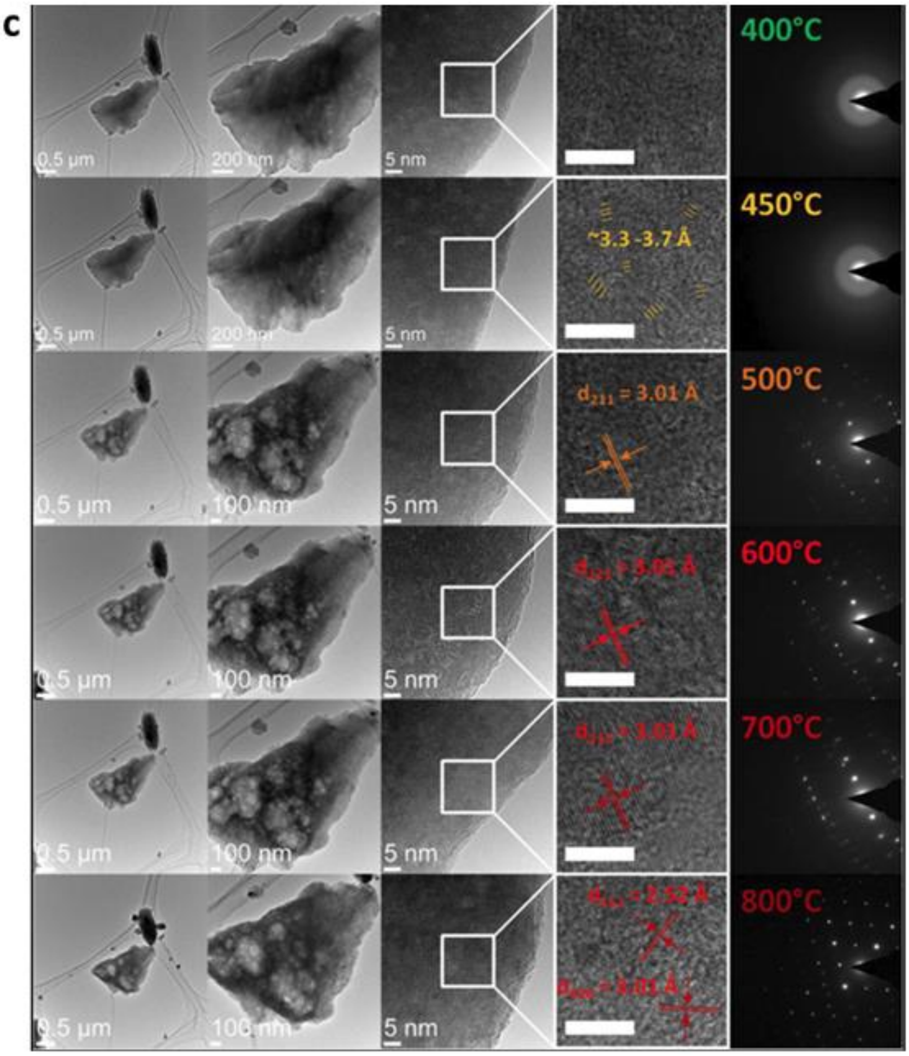

Figure 21. In-situ XRD of $LiFePO_4$ heated under inert atmosphere. (a) 435–700 °C. (**b**) From RT to 900 °C and then cooling to RT. (**c**) In-situ TEM of a $LiFePO_4$ particle heated between 400 and 800 °C. The first two columns show TEM images of the same grain; the third and fourth show HRTEM images, the fifth shows SAED patterns in the same region. Notice a slight grain rotation at 800 °C compared with 700 °C and lower temperatures, which resulted in a change of the zone axis, a different SAED pattern, and different planes visible in HRTEM images [199]; with permission of the ACS.

3.4.2. Phase Evolution of $LiFePO_4$ Precursor

A composite material consisting of carbon-coated $LiMn_{0.75}Fe_{0.25}PO_4$ nanoparticles within a 3D graphene micro-spherical is produced using a salt-assisted spray drying method. The goal is to improve the electrochemical properties of $LiMn_{0.75}Fe_{0.25}PO_4$ by enhancing its electronic conductivity and Li^+ diffusivity. The composite is synthesized by a spray-drying process using a solution mixture of chelated metal salts and subsequent heat treatment.

The phase evolution of the 3D $LiMn_{0.75}Fe_{0.25}PO_4$/reduced graphene oxide (rGO) microspheres during heat treatment between 100 and 650 °C in an inert atmosphere is monitored by in-situ XRD; the development of the XRD patterns is shown in Figure 22 [18]. The as-spray-dried precursor is amorphous, see spectrum at 30 °C. The as-spray-dried precursor is then dried at 100 °C and becomes crystalline, with the pattern corresponding to a mixture of MCl_2 (M = Fe and Mn) and LiH_2PO_4. When the temperature is increased to 280 °C, MPO_4 and Li_3PO_4 phases are formed. Upon heating to 450 °C, an olivine $LiMPO_4$ is observed, together with MPO_4. Upon further temperature increase to 650 °C, single-phase $LiMn_{0.75}Fe_{0.25}PO_4$ is obtained at the expense of the MPO_4 phase. The result indicates that the maximum temperature required for achieve a single phase is ~650 °C. This in-situ XRD result indicates the $LiMn_{0.75}Fe_{0.25}PO_4$ phase formation path as follows:

30–100 °C: $Li\text{-}Mn\text{-}Fe\text{-}PO_4/GO$ precursor → $(Mn/Fe)Cl_2$ + $(Mn/Fe)PO_4$ + Li containing phase
100–280 °C: $(Mn/Fe)Cl_2$ +$(Mn/Fe)PO_4$ + Li containing phase → Li_3PO_4 + $(Mn/Fe)PO_4$
280–450 °C: Li_3PO_4 + $(Mn/Fe)PO_4$ → $Li(Mn/Fe)PO_4$
450–650 °C: $(Mn/Fe)PO_4$ + Li containing phase → $Li(Mn/Fe)PO_4$ (single phase)

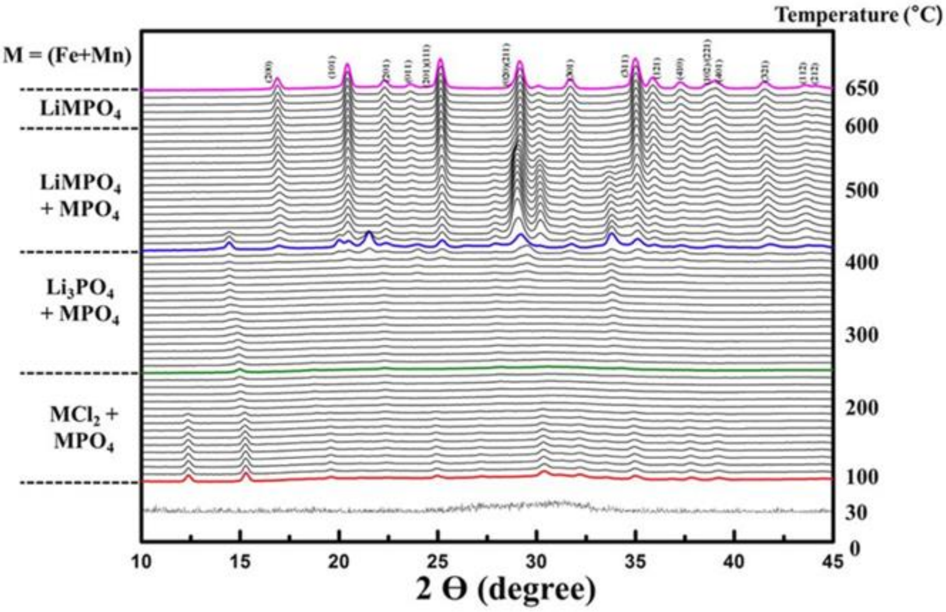

Figure 22. In-situ X-ray diffraction patterns of the $Li\text{-}Mn\text{-}Fe\text{-}PO_4/GO$ precursor prepared using the metal chlorides heated from 100 to 650 °C in an inert atmosphere [18], with permission from Springer Nature.

The 3D $LiMn_{0.75}Fe_{0.25}PO_4/rGO$ microspheres that were synthesized exhibit a high tap density, high specific capacity, excellent rate capability, and superior cycling stability as a cathode material for lithium-ion batteries.

4. Conclusions

With the advances of X-ray diffractometer as well as the availability of synchrotron diffractometer, the operando X-ray diffraction technique is now widely used to explore various aspects of lithium/sodium-ion batteries, including: (a) the working mechanisms of electrodes, as well as the influences of particle size of the electrode material, the cycling current and the composition on the working mechanism; (b) the impact of overcharge on the electrode materials; (c) the thermal stability of the electrodes; (d) the degradation mechanism and (e) the synthesis of the materials. The information obtained from the operando XRD investigations make it possible to have an atomic level understanding on how the rechargeable batteries work in relation to their crystal structure, why they behave in their specific ways, how to change the undesired working mechanisms, how and why they fail, as well as the optimized conditions to produce the high quality materials. To improve the existing electrode materials and the design of new high performance ones, not only is the structure information of the collective materials obtained from XRD important, but also the local information on the atomic level. Thus, operando XRD should be developed in the direction of combining with other techniques to allow collecting different types of information simultaneously. Presently, XRD-MS, XRD-DSC, XRD-XAS, etc. are used in material research, but more multi-function instruments with rapid measurement/fast data collection are required. In addition, it is important to develop operando techniques with the capability of obtaining 3D crystal structure, as well as 3D morphology information of the electrodes, which is essential for improving electrode quality. Finally, the operando techniques should be able to measure the desired materials in the same environment and conditions as the battery in practical applications.

Author Contributions: W.Z. wrote the draft. All authors contributed to the writing, discussion and revision of the final version.

Funding: This research received no external funding.

Conflicts of Interest: All the authors declare no competing interests.

References

1. Etacheri, V.; Marom, R.; Elazari, R.; Salitraa, G.; Aurbach, D. Challenges in the development of advanced Li-ion batteries: a review. *Energy Environ. Sci.* **2011**, *4*, 3243–3262. [CrossRef]
2. Wen, J.; Yu, Y.; Chen, C. A Review on Lithium-Ion Batteries Safety Issues: Existing Problems and Possible Solutions. *Mater. Express* **2012**, *2*, 197–212. [CrossRef]
3. Armand, M.; Tarascon, J.-M. Building better batteries. *Nature* **2008**, *451*, 652–657. [CrossRef] [PubMed]
4. Li, Y.; Lu, Y.; Zhao, C.; Hu, Y.-S.; Titirici, M.-M.; Li, H.; Huang, X.; Chen, L. Recent advances of electrode materials for low-cost sodium-ion batteries towards practical application for grid energy storage. *Energy Storage Mater.* **2017**, *7*, 130–151. [CrossRef]
5. Nitta, N.; Wu, F.; Lee, J.T.; Yushin, G. Li-ion battery materials: present and future. *Mater. Today* **2015**, *18*, 252–264. [CrossRef]
6. Meng, J.; Guo, H.; Niu, C.; Zhao, Y.; Xu, L.; Li, Q.; Mai, L. Advances in Structure and Property Optimizations of Battery Electrode Materials. *Joule* **2017**, *1*, 522–547. [CrossRef]
7. Ding, Y.; Wang, R.; Wang, L.; Cheng, K.; Zhao, Z.; Mu, D.; Wu, B. A Short Review on Layered $LiNi_{0.8}Co_{0.1}Mn_{0.1}O_2$ Positive Electrode Material for Lithium-ion Batteries. *Energy Procedia* **2017**, *105*, 2941–2952. [CrossRef]
8. Ding, Y.; Mu, D.; Wu, B.; Wang, R.; Zhao, Z.; Wu, F. Recent progresses on nickel-rich layered oxide positive electrode materials used in lithium-ion batteries for electric vehicles. *Appl. Energy* **2017**, *195*, 586–599. [CrossRef]
9. Manivannan, V.; Chennabasappa, M.; Garrett, J. Optimization and Characterization of Lithium Ion Cathode Materials in the System $(1 - x - y)LiNi_{0.8}Co_{0.2}O_2 \bullet xLi_2MnO_3 \bullet yLiCoO_2$. *Energies* **2010**, *3*, 847–866. [CrossRef]
10. Rozier, P.; Tarascon, J.M. Review—Li-Rich Layered Oxide Cathodes for Next-Generation Li-Ion Batteries: Chances and Challenges. *J. Electrochem. Soc.* **2015**, *162*, A2490–A2499. [CrossRef]
11. Liu, Q.; Wang, S.; Tan, H.; Yang, Z.; Zeng, J. Preparation and Doping Mode of Doped $LiMn_2O_4$ for Li-Ion Batteries. *Energies* **2013**, *6*, 1718–1730. [CrossRef]
12. Zhu, W.; Liu, D.; Trottier, J.; Gagnon, C.; Guerfi, A.; Julien, C.M.; Mauger, A.; Zaghib, K. Comparative studies of the phase evolution in M-doped $LixMn_{1.5}Ni_{0.5}O_4$ (M = Co, Al, Cu and Mg) by in-situ X-ray diffraction. *J. Power Sources* **2014**, *264*, 290–298. [CrossRef]
13. Yang, J.; Han, X.; Zhang, X.; Cheng, F.; Chen, J. Spinel $LiNi_{0.5}Mn_{1.5}O_4$ cathode for rechargeable lithiumion batteries: Nano vs micro, ordered phase (P4332) vs disordered phase (Fd3-m). *Nano Res.* **2013**, *6*, 679–687. [CrossRef]
14. Liu, D.; Lu, Y.; Goodenough, J.B. Rate Properties and Elevated-Temperature Performances of $LiNi_{0.5-x}Cr_{2x}Mn_{1.5-x}O_4$ ($0 \leq 2x \leq 0.8$) as 5 V Cathode Materials for Lithium-Ion Batteries. *J. Electrochem. Soc.* **2010**, *157*, A1269. [CrossRef]
15. Dimesso, L.; Forster, C.; Jaegermann, W.; Khanderi, J.P.; Tempel, H.; Popp, A.; Engstler, J.; Schneider, J.J.; Sarapulova, A.; Mikhailova, D.; et al. Developments in nanostructured LiMPO4 (M = Fe, Co, Ni, Mn) composites based on three dimensional carbon architecture. *Chem. Soc. Rev.* **2012**, *41*, 5068–5680. [CrossRef] [PubMed]
16. Shin, H.C.; Nam, K.W.; Chang, W.Y.; Cho, B.W.; Yoon, W.-S.; Yang, X.-Q.; Chung, K.Y. Comparative studies on C-coated and uncoated $LiFePO_4$ cycling at various rates and temperatures using synchrotron based in situ X-ray diffraction. *Electrochim. Acta* **2011**, *56*, 1182–1189. [CrossRef]
17. Joachin, H.; Kaun, T.D.; Zaghib, K.; Prakasha, J. Electrochemical and Thermal Studies of Carbon-Coated LiFePO4 Cathode. *J. Electrochem. Soc.* **2009**, *156*, A401–A406. [CrossRef]

18. Kim, M.-S.; Kim, H.-K.; Lee, S.-W.; Kim, D.-H.; Ruan, D.; Chung, K.Y.; Lee, S.H.; Roh, K.C.; Kim, K.-B. Synthesis of Reduced Graphene Oxide-Modified $LiMn_{0.75}Fe_{0.25}PO_4$ Microspheres by Salt-Assisted Spray Drying for High-Performance Lithium-Ion Batteries. *Sci. Rep.* **2016**, *6*, 26686. [CrossRef] [PubMed]
19. Liu, D.; Zhu, W.; Kim, C.; Cho, M.; Guerfi, A.; Delp, S.A.; Allen, J.L.; Jow, T.R.; Zaghib, K. High-energy lithium-ion battery using substituted $LiCoPO_4$: From coin type to 1 Ah cell. *J. Power Sources* **2018**, *388*, 52–56. [CrossRef]
20. Vijaya Babu, K.; Seeta Devi, L.; Veeraiah, V.; Anand, K. Structural and dielectric studies of $LiNiPO_4$ and $LiNi_{0.5}Co_{0.5}PO_4$ cathode materials for lithium-ion batteries. *J. Asian Ceram. Soc.* **2016**, *4*, 269–276. [CrossRef]
21. Qi, X.; Wang, Y.; Jiang, L.; Mu, L.; Zhao, C.; Liu, L.; Hu, Y.-S.; Chen, L.; Huang, X. Sodium-Deficient O3-$Na_{0.9}[Ni_{0.4}Mn_xTi_{0.6-x}]O_2$ Layered-Oxide Cathode Materials for Sodium-Ion Batteries. *Part. Part. Syst. Charact.* **2015**, *33*, 538–544. [CrossRef]
22. Mu, L.; Xu, S.; Li, Y.; Hu, Y.-S.; Li, H.; Chen, L.; Huang, X. Prototype Sodium-Ion Batteries Using an Air-Stable and Co/Ni-Free O3-Layered Metal Oxide Cathode. *Adv. Mater.* **2015**, *27*, 6928–6933. [CrossRef] [PubMed]
23. Kim, J.; Seo, D.-H.; Kim, H.; Park, I.; Yoo, J.-K.; Jung, S.-K.; Park, Y.-U.; Goddard, W.A., III; Kang, K. Unexpected discovery of low-cost maricite $NaFePO_4$ as a high-performance electrode for Na-ion batteries. *Energy Environ. Sci.* **2015**, *8*, 540–545. [CrossRef]
24. Jian, Z.; Han, W.; Lu, X.; Yang, H.; Hu, Y.-S.; Zhou, J.; Zhou, Z.; Li, J.; Chen, W.; Chen, D.; Chen, L. Superior Electrochemical Performance and Storage Mechanism of $Na_3V_2(PO_4)_3$ Cathode for Room-Temperature Sodium-Ion Batteries. *Adv. Energy Mater.* **2012**, *3*, 156–160. [CrossRef]
25. Zhou, W.; Xue, L.; Lü, X.; Gao, H.; Li, Y.; Xin, S.; Fu, G.; Cui, Z.; Zhu, Y.; Goodenough, J.B. $NaxMV(PO_4)_3$ (M = Mn, Fe, Ni) Structure and Properties for Sodium Extraction. *Nano Lett.* **2016**, *16*, 7836–7841. [CrossRef] [PubMed]
26. Aurbach, D.; Markovsky, B.; Weissman, I.; Levi, E.; Ein-Eli, Y. On the correlation between surface chemistry and performance of graphite negative electrodes for Li ion batteries. *Electrochim. Acta* **1999**, *45*, 67–86. [CrossRef]
27. Wang, Y.; Feng, Z.; Zhu, W.; Gariépy, V.; Gagnon, C.; Provencher, M.; Laul, D.; Veillette, R.; Trudeau, M.; Guerfi, A.; et al. High Capacity and High Efficiency Maple Tree-Biomass-Derived Hard Carbon as an Anode Material for Sodium-Ion Batteries. *Materials* **2018**, *11*, 1294. [CrossRef] [PubMed]
28. Wang, K.; Jin, Y.; Sun, S.; Huang, Y.; Peng, J.; Luo, J.; Zhang, Q.; Qiu, Y.; Fang, C.; Han, J. Low-Cost and High-Performance Hard Carbon Anode Materials for Sodium-Ion Batteries. *ACS Omega* **2017**, *2*, 1687–1695. [CrossRef]
29. He, Y.-B.; Li, B.; Liu, M.; Zhang, C.; Lv, W.; Yang, C.; Li, J.; Du, H.; Zhang, B.; Yang, Q.-H.; et al. Gassing in $Li_4Ti_5O_{12}$-based batteries and its remedy. *Sci. Rep.* **2012**, *2*, 913. [CrossRef] [PubMed]
30. Han, X.; Ouyang, M.; Lu, L.; Li, J. Cycle Life of Commercial Lithium-Ion Batteries with Lithium Titanium Oxide Anodes in Electric Vehicles. *Energies* **2014**, *7*, 4896–4909. [CrossRef]
31. Wen, Y.; He, K.; Zhu, Y.; Han, F.; Xu, Y.; Matsuda, I.; Ishii, Y.; Cumings, J.; Wang, C. Expanded graphite as superior anode for sodium-ion batteries. *Nat. Commun.* **2014**, *5*, 4033. [CrossRef] [PubMed]
32. Zhang, J.; Lv, W.; Tao, Y.; He, Y.-B.; Wang, D.-W.; You, C.-H.; Li, B.; Kang, F.; Yang, Q.-H. Ultrafast high-volumetric sodium storage of folded-graphene electrodes through surface-induced redox reactions. *Energy Storage Mater.* **2015**, *1*, 112–118. [CrossRef]
33. Liu, S.; Lei, W.; Liu, Y.; Zhang, W.-H. Uniform ReS_2 porous nanospheres assembled from curly ReS_2 few-layers with an expanded interlayer spacing for high-performance lithium-ion batteries. *Chem. Eng. J.* **2019**, *357*, 112–119. [CrossRef]
34. Bella, F.; Muñoz-García, A.B.; Colò, F.; Meligrana, G.; Lamberti, A.; Destro, M.; Pavone, M.; Gerbaldi, C. Combined Structural, Chemometric, and Electrochemical Investigation of Vertically Aligned TiO_2 Nanotubes for Na-ion Batteries. *ACS Omega* **2018**, *3*, 8440–8450. [CrossRef]
35. Wang, H.; Jiang, Y.; Manthiram, A. N-doped Fe3C@C as an efficient polyselenide reservoir for high-performance sodium-selenium batteries. *Energy Storage Mater.* **2019**, *16*, 374–382. [CrossRef]
36. Xu, K. Electrolytes and interphases in Li-ion batteries and beyond. *Chem. Rev.* **2014**, *114*, 11503–11618. [CrossRef] [PubMed]
37. Zheng, J.; Lochala, J.A.; Kwok, A.; Deng, Z.D.; Xiao, J. Research Progress towards Understanding the Unique Interfaces between Concentrated Electrolytes and Electrodes for Energy Storage Applications. *Adv. Sci.* **2017**, *4*, 1700032. [CrossRef] [PubMed]

38. Scheers, J.; Fantini, S.; Johansson, P. A review of electrolytes for lithium–sulphur batteries. *J. Power Sources* **2014**, *255*, 204–218. [CrossRef]
39. Erickson, E.M.; Markevich, E.; Salitra, G.; Sharon, D.; Hirshberg, D.; de la Llave, E.; Shterenberg, I.; Rozenman, A.; Frimer, A.; Aurbach, D. Review—Development of Advanced Rechargeable Batteries: A Continuous Challenge in the Choice of Suitable Electrolyte Solutions. *J. Electrochem. Soc.* **2015**, *162*, A2424–A2438. [CrossRef]
40. Cheng, X.B.; Zhang, R.; Zhao, C.Z.; Wei, F.; Zhang, J.G.; Zhang, Q. A Review of Solid Electrolyte Interphases on Lithium Metal Anode. *Adv. Sci.* **2016**, *3*, 1500213. [CrossRef] [PubMed]
41. Zhou, Q.; Henderson, W.A.; Appetecchi, G.B.; Montanino, M.; Passerini, S. Physical and Electrochemical Properties of *N*-Alkyl-*N*-methylpyrrolidinium Bis(fluorosulfonyl)imide Ionic Liquids: PY13FSI and PY14FSI. *J. Phys. Chem. B* **2008**, *112*, 13577–13580. [CrossRef] [PubMed]
42. Nazet, A.; Sokolov, S.; Sonnleitner, T.; Makino, T.; Kanakubo, M.; Buchner, R. Densities, Viscosities, and Conductivities of the Imidazolium Ionic Liquids [Emim][Ac], [Emim][FAP], [Bmim][BETI], [Bmim][FSI], [Hmim][TFSI], and [Omim][TFSI]. *J. Chem. Eng. Data* **2015**, *60*, 2400–2411. [CrossRef]
43. Moreno, M.; Simonetti, E.; Appetecchi, G.B.; Carewska, M.; Montanino, M.; Kim, G.T.; Loeffler, N.; Passerini, S. Ionic Liquid Electrolytes for Safer Lithium Batteries. *J. Electrochem. Soc.* **2016**, *164*, A6026–A6031. [CrossRef]
44. Marczewski, M.J.; Stanje, B.; Hanzu, I.; Wilkening, M.; Johansson, P. "Ionic liquids-in-salt"—A promising electrolyte concept for high-temperature lithium batteries? *Phys. Chem. Chem. Phys.* **2014**, *16*, 12341–12349. [CrossRef] [PubMed]
45. Colò, F.; Bella, F.; Nair, J.R.; Gerbaldi, C. Light-cured polymer electrolytes for safe, low-cost and sustainable sodium-ion batteries. *J. Power Sources* **2017**, *365*, 293–302. [CrossRef]
46. Edman, L. Ion Association and Ion Solvation Effects at the Crystalline−Amorphous Phase Transition in PEO−LiTFSI. *J. Phys. Chem. B* **2000**, *104*, 7254–7258. [CrossRef]
47. Das, S.; Ghosh, A. Structure, ion transport, and relaxation dynamics of polyethylene oxide/poly (vinylidene fluoride co-hexafluoropropylene)—lithium bis(trifluoromethane sulfonyl) imide blend polymer electrolyte embedded with ionic liquid. *J. Appl. Phys.* **2016**, *119*, 095101. [CrossRef]
48. Chan, C.K.; Yang, T.; Mark Weller, J. Nanostructured Garnet-type $Li_7La_3Zr_2O_{12}$: Synthesis, Properties, and Opportunities as Electrolytes for Li-ion Batteries. *Electrochim. Acta* **2017**, *253*, 268–280. [CrossRef]
49. Wu, J.-F.; Chen, E.-Y.; Yu, Y.; Liu, L.; Wu, Y.; Pang, W.K.; Peterson, V.K.; Guo, X. Gallium-Doped $Li_7La_3Zr_2O_{12}$ Garnet-Type Electrolytes with High Lithium-Ion Conductivity. *ACS Appl. Mater. Inter.* **2017**, *9*, 1542–1552. [CrossRef] [PubMed]
50. Xie, H.; Li, Y.; Goodenough, J.B. Low-temperature synthesis of $Li_7La_3Zr_2O_{12}$ with cubic garnet-type structure. *Mater. Res. Bull.* **2012**, *47*, 1229–1232. [CrossRef]
51. Ooms, F.G.B.; Wagemaker, M.; van Well, A.A.; Mulder, F.M.; Kelder, E.M.; Schoonman, J. Structure determination of high-voltage $LiMg_{\delta}Ni_{0.5-\delta}Mn_{1.5}O_4$ spinels for Li-ion batteries. *Appl. Phys. A* **2002**, *74*, s1089–s1091. [CrossRef]
52. Fürtauer, S.; Effenberger, H.S.; Flandorfer, H. $CuLi_2Sn$ and Cu_2LiSn: Characterization by single crystal XRD and structural discussion towards new anode materials for Li-ion batteries. *J. Solid State Chem.* **2014**, *220*, 198–205. [CrossRef] [PubMed]
53. Boivin, E.; Masquelier, C.; Croguennec, L.; Chotard, J.-N. Crystal Structure and Lithium Diffusion Pathways of a Potential Positive Electrode Material for Lithium-Ion Batteries: $Li_2VIII(H_{0.5}PO_4)_2$. *Inorg. Chem.* **2017**, *56*, 6776–6779. [CrossRef] [PubMed]
54. Reimers, J.N.; Dahn, J.R. Electrochemical and In Situ X-ray Diffraction Studies of Lithium Intercalation in $LixCo0_2$. *J. Electrochem. Soc.* **1992**, *139*, 2091–2097. [CrossRef]
55. Whitehead, A.H.; Edstrtim, K.; Rao, N.; Owen, J.R. In situ X-ray diffraction studies of a graphite-based Li-ion battery negative electrode. *J. Power Sources* **1996**, *63*, 41–45. [CrossRef]
56. Yang, X.Q.; McBreen, J.; Yoon, W.-W.; Grey, C.P. Crystal structure changes of $LiMn_{0.5}Ni_{0.5}O_2$ cathode materials during charge and discharge studied by synchrotron based in situ XRD. *Electrochem. Commun.* **2002**, *4*, 649–654. [CrossRef]
57. Zhang, X.; Kuhnel, R.-S.; Schroeder, M.; Balducci, A. Revisiting $Li_3V_2(PO_4)_3$ as an anode—An outstanding negative electrode for high power energy storage devices. *J. Mater. Chem. Phys.* **2014**, *2*, 17906–17913. [CrossRef]

58. Wang, H.; Wang, F. In situ, operando measurements of rechargeable batteries. *Curr. Opin. Chem. Eng.* **2016**, *13*, 170–178. [CrossRef]
59. Zhang, G.; Xiong, T.; He, L.; Yan, M.; Zhao, K.; Xu, X.; Mai, L. Electrochemical in situ X-ray probing in lithium-ion and sodium-ion batteries. *J. Mater. Sci.* **2017**, *52*, 3697–3718. [CrossRef]
60. Sun, Y.; Zhao, L.; Pan, H.; Lu, X.; Gu, L.; Hu, Y.S.; Li, H.; Armand, M.; Ikuhara, Y.; Chen, L.; et al. Direct atomic-scale confirmation of three-phase storage mechanism in $Li_4Ti_5O_{12}$ anodes for room-temperature sodium-ion batteries. *Nat. Commun.* **2013**, *4*, 1870. [CrossRef] [PubMed]
61. Bobrikov, I.A.; Samoylova, N.Y.; Sumnikov, S.V.; Ivanshina, O.Y.; Vasin, R.N.; Beskrovnyi, A.I.; Balagurov, A.M. In-situ time-of-flight neutron diffraction study of the structure evolution of electrode materials in a commercial battery with $LiNi_{0.8}Co_{0.15}Al_{0.05}O_2$ cathode. *J. Power Sources* **2017**, *372*, 74–81. [CrossRef]
62. Dolotko, O.; Senyshyn, A.; Mühlbauer, M.J.; Nikolowski, K.; Ehrenberg, H. Understanding structural changes in NMC Li-ion cells by in situ neutron diffraction. *J. Power Sources* **2014**, *255*, 197–203. [CrossRef]
63. Li, J.; Petibon, R.; Glazier, S.; Sharma, N.; Pang, W.K.; Peterson, V.K.; Dahn, J.R. In-situ Neutron Diffraction Study of a High Voltage $Li(Ni_{0.42}Mn_{0.42}Co_{0.16})O_2$/Graphite Pouch Cell. *Electrochim. Acta* **2015**, *180*, 234–240. [CrossRef]
64. Wang, X.L.; An, K.; Cai, L.; Feng, Z.; Nagler, S.E.; Daniel, C.; Rhodes, K.J.; Stoica, A.D.; Skorpenske, H.D.; Liang, C.; et al. Visualizing the chemistry and structure dynamics in lithium-ion batteries by in-situ neutron diffraction. *Sci. Rep.* **2012**, *2*, 747. [CrossRef] [PubMed]
65. Bobrikova, I.A.; Hub, C.W.; Lee, C.H.; Chenb, T.Y.; Deleg, S.; Balagurova, D.A. Structural evolution in $LiFePO_4$-based battery materials: In-situ and ex-situ time-of-flight neutron diffraction study. *J. Power Sources* **2014**, *258*, 356–364. [CrossRef]
66. Sottmann, J.; DiMichiel, M.; Fjellvåg, H.; Malavasi, L.; Margadonna, S.; Vajeeston, P.; Vaughan, G.B.M.; Wragg, D.S. Chemical Structures of Specific Sodium Ion Battery Components Determined by Operando Pair Distribution Function and X-ray Diffraction Computed Tomography. *Angew. Chem. Int. Edit.* **2017**, *56*, 11385–11389. [CrossRef] [PubMed]
67. Wang, J.; Chen-Wiegart, Y.-C.K.; Wang, J. In operando tracking phase transformation evolution of lithium iron phosphate with hard X-ray microscopy. *Nat. Commun.* **2014**, *5*, 4570. [CrossRef] [PubMed]
68. Chan, H.-W.; Duh, J.-G.; Lee, J.-F. Valence change by in situ XAS in surface modified $LiMn_2O_4$ for Li-ion battery. *Electrochem. Commun.* **2006**, *8*, 1731–1736. [CrossRef]
69. Dominko, R.; Arčon, I.; Kodre, A.; Hanžel, D.; Gaberšček, M. In-situ XAS study on Li_2MnSiO_4 and Li_2FeSiO_4 cathode materials. *J. Power Sources* **2009**, *189*, 51–58. [CrossRef]
70. Fehse, M.; Monconduit, L.; Fischer, F.; Tessier, C.; Stievano, L. Study of the insertion mechanism of lithium into anatase by operando X-ray diffraction and absorption spectroscopy. *Solid State Ion.* **2014**, *268*, 252–255. [CrossRef]
71. Giorgetti, M. A Review on the Structural Studies of Batteries and Host Materials by X-ray Absorption Spectroscopy. *ISRN Mater. Sci.* **2013**, *2013*, 1–22. [CrossRef]
72. Giuliana, A.; Marco, G.; Robert, D.; Lorenzo, S.; Iztok, A.; Nicola, N.; Luca, O. Operando characterization of batteries using X-ray absorption spectroscopy: Advances at the beamline XAFS at synchrotron Elettra. *J. Phys. D Appl. Phys.* **2017**, *50*, 074001. [CrossRef]
73. Menzel, M.; Schlifke, A.; Falk, M.; Janek, J.; Fröba, M.; Fittschen, U.E.A. Surface and in-depth characterization of lithium-ion battery cathodes at different cycle states using confocal micro-X-ray fluorescence-X-ray absorption near edge structure analysis. *Spectrochim. Acta B* **2013**, *85*, 62–70. [CrossRef]
74. Dokko, K.; Mohamedi, M.; Anzue, N.; Itoh, T.; Uchida, I. In situ Raman spectroscopic studies of $LiNixMn_{2-x}O_4$thin film cathode materials for lithium ion secondary batteries. *J. Mater. Chem.* **2002**, *12*, 3688–3693. [CrossRef]
75. Hardwick, L.J.; Ruch, P.W.; Hahn, M.; Scheifele, W.; Kötz, R.; Novák, P. In situ Raman spectroscopy of insertion electrodes for lithium-ion batteries and supercapacitors: First cycle effects. *J. Phys. Chem. Solids* **2008**, *69*, 1232–1237. [CrossRef]
76. Wu, J.; Dathar, G.K.; Sun, C.; Theivanayagam, M.G.; Applestone, D.; Dylla, A.G.; Manthiram, A.; Henkelman, G.; Goodenough, J.B.; Stevenson, K.J. In situ Raman spectroscopy of LiFePO4: size and morphology dependence during charge and self-discharge. *Nanotechnology* **2013**, *24*, 9. [CrossRef] [PubMed]

77. Membreno, N.; Xiao, P.; Park, K.S.; Goodenough, J.B.; Henkelman, G.; Stevenso, K.J. In Situ Raman Study of Phase Stability of α-$Li_3V_2(PO_4)_3$ upon Thermal and Laser Heating. *J. Phys. Chem. C* **2013**, *117*, 11994–12002. [CrossRef]
78. Stancovski, V.; Badilescu, S. In situ Raman spectroscopic–electrochemical studies of lithium-ion battery materials: a historical overview. *J. Appl. Electrochem.* **2014**, *44*, 23–43. [CrossRef]
79. Aurbach, D.; Chusid, O. The use of in situ Fourier-transform infrared spectroscopy for the study of surface phenomena on electrodes in selected lithium battery electrolyte solutions. *J. Power Sources* **1997**, *68*, 463–470. [CrossRef]
80. Cheng, H.; Zhu, C.B.; Lu, M.; Yang, Y. In situ micro-FTIR study of the solid–solid interface between lithium electrode and polymer electrolytes. *J. Power Sources* **2007**, *174*, 1027–1031. [CrossRef]
81. Chusid, O.; Gofer, Y.; Aurbach, D.; Watanabe, M.; Momma, T.; Osaka, T. Studies of the interface between lithium electrodes and polymeric electrolyte systems using in situ FTIR spectroscopy. *J. Power Sources* **2001**, *97–98*, 632–636. [CrossRef]
82. Ye, J.-Y.; Jiang, Y.-X.; Sheng, T.; Sun, S.-G. In-situ FTIR spectroscopic studies of electrocatalytic reactions and processes. *Nano Energy* **2016**, *29*, 414–427. [CrossRef]
83. Hovington, P.; Dontigny, M.; Guerfi, A.; Trottier, J.; Lagacé, M.; Mauger, A.; Julien, C.M.; Zaghib, K. In situ Scanning electron microscope study and microstructural evolution of nano silicon anode for high energy Li-ion batteries. *J. Power Sources* **2014**, *248*, 457–464. [CrossRef]
84. Marceau, H.; Kim, C.-S.; Paolella, A.; Ladouceur, S.; Lagacé, M.; Chaker, M.; Vijh, A.; Guerfi, A.; Julien, C.M.; Mauger, A.; et al. In operando scanning electron microscopy and ultraviolet–visible spectroscopy studies of lithium/sulfur cells using all solid-state polymer electrolyte. *J. Power Sources* **2016**, *319*, 247–254. [CrossRef]
85. Miller, D.J.; Proff, C.; Wen, J.G.; Abraham, D.P.; Bareño, J. Observation of Microstructural Evolution in Li Battery Cathode Oxide Particles by In Situ Electron Microscopy. *Adv. Energy Mater.* **2013**, *3*, 1098–1103. [CrossRef]
86. Liu, S.; Xie, J.; Su, Q.; Du, G.; Zhang, S.; Cao, G.; Zhu, T.; Zhao, X. Understanding Li-storage mechanism and performance of $MnFe_2O_4$ by in situ TEM observation on its electrochemical process in nano lithium battery. *Nano Energy* **2014**, *8*, 84–94. [CrossRef]
87. Chen, K.; Cao, K.; Xing, C.; Hu, Y.; Liu, J.; He, Y.; Wang, J.; Li, A.; Qin, H. In-situ TEM study of the lithiation and delithiation of FeS nanosheets. *J. Alloy. Compd.* **2016**, *688*, 946–952. [CrossRef]
88. Janish, M.T.; Carter, C.B. In situ TEM observations of the lithiation of molybdenum disulfide. *Scr. Mater.* **2015**, *107*, 22–25. [CrossRef]
89. Wang, C.M. In situ transmission electron microscopy and spectroscopy studies of rechargeable batteries under dynamic operating conditions: A retrospective and perspective view. *J. Mater. Res.* **2015**, *30*, 326–339. [CrossRef]
90. Xu, Z.-L.; Cao, K.; Abouali, S.; Akbari Garakani, M.; Huang, J.; Huang, J.-Q.; Kamali Heidari, E.; Wang, H.; Kim, J.-K. Study of lithiation mechanisms of high performance carbon-coated Si anodes by in-situ microscopy. *Energy Storage Mater.* **2016**, *3*, 45–54. [CrossRef]
91. Zhu, Y.; Wang, J.W.; Liu, Y.; Liu, X.; Kushima, A.; Liu, Y.; Xu, Y.; Mao, S.X.; Li, J.; Wang, C.; et al. In Situ Atomic-Scale Imaging of Phase Boundary Migration in $FePO_4$ Microparticles During Electrochemical Lithiation. *Adv. Mater.* **2013**, *25*, 5461–5466. [CrossRef] [PubMed]
92. Orikasa, Y.; Maeda, T.; Koyama, Y.; Murayama, H.; Fukuda, K.; Tanida, H.; Arai, H.; Matsubara, E.; Uchimoto, Y.; Ogumi, Z. Direct Observation of a Metastable Crystal Phase of Li_xFePO_4 under Electrochemical Phase Transition. *J. Am. Chem. Soc.* **2013**, *135*, 5497–5500. [CrossRef] [PubMed]
93. Bak, S.-M.; Hu, E.; Zhou, Y.; Yu, X.; Senanayake, S.D.; Cho, S.-J.; Kim, K.-B.; Chung, K.Y.; Yang, X.-Q.; Nam, K.-W. Structural Changes and Thermal Stability of Charged $LiNi_xMn_yCo_zO_2$ Cathode Materials Studied by Combined In Situ Time-Resolved XRD and Mass Spectroscopy. *ACS Appl. Mater. Interfaces* **2014**, *6*, 22594–22601. [CrossRef] [PubMed]
94. Li, J.; Shunmugasundaram, R.; Doig, R.; Dahn, J.R. In Situ X-ray Diffraction Study of Layered Li–Ni–Mn–Co Oxides: Effect of Particle Size and Structural Stability of Core–Shell Materials. *Chem. Mater.* **2016**, *28*, 162–171. [CrossRef]
95. Kim, H.; Hong, J.; Yoon, G.; Kim, H.; Park, K.-Y.; Park, M.-S.; Yoon, W.-S.; Kang, K. Sodium intercalation chemistry in graphite. *Energy Environ. Sci.* **2015**, *8*, 2963–2969. [CrossRef]

96. Wang, P.-F.; Yao, H.-R.; Liu, X.-Y.; Yin, Y.-X.; Zhang, J.-N.; Wen, Y.; Yu, X.; Gu, L.; Guo, Y.-G. Na^+/vacancy disordering promises high-rate Na-ion batteries. *Sci. Adv.* **2018**, *4*, eaar6018. [CrossRef] [PubMed]
97. Qiu, S.; Xiao, L.; Sushko, M.L.; Han, K.S.; Shao, Y.; Yan, M.; Liang, X.; Mai, L.; Feng, F.; Cao, Y.; et al. Manipulating Adsorption–Insertion Mechanisms in Nanostructured Carbon Materials for High-Efficiency Sodium Ion Storage. *Adv. Energy Mater.* **2017**, *7*, 1700403. [CrossRef]
98. Bock, D.C.; Pelliccione, C.J.; Zhang, W.; Timoshenko, J.; Knehr, K.W.; West, A.C.; Wang, F.; Li, Y.; Frenkel, A.I.; Takeuchi, E.S.; et al. Size dependent behavior of Fe_3O_4 crystals during electrochemical (de)lithiation: An in situ X-ray diffraction, ex situ X-ray absorption spectroscopy, transmission electron microscopy and theoretical investigation. *Phys. Chem. Chem. Phys.* **2017**, *19*, 20867–20880. [CrossRef] [PubMed]
99. Yu, X.; Pan, H.; Wan, W.; Ma, M.; Bai, J.; Meng, Q.; Ehrlich, S.N.; Hu, Y.S.; Yang, X.Q. A Size-Dependent Sodium Storage Mechanism in $Li_4Ti_5O_{12}$ Investigated by a Novel Characterization Technique Combining in Situ X-ray Diffraction and Chemical Sodiation. *Nano Lett.* **2013**, *13*, 4721–4727. [CrossRef] [PubMed]
100. Orikasa, Y.; Maeda, T.; Koyama, Y.; Murayama, H.; Fukuda, K.; Tanida, H.; Arai, H.; Matsubara, E.; Uchimoto, Y.; Ogumi, Z. Transient Phase Change in Two Phase Reaction between $LiFePO_4$ and $FePO_4$ under Battery Operation. *Chem. Mater.* **2013**, *25*, 1032–1039. [CrossRef]
101. Fell, C.R.; Chi, M.; Meng, Y.S.; Jones, J.L. In situ X-ray diffraction study of the lithium excess layered oxide compound $Li[Li_{0.2}Ni_{0.2}Mn_{0.6}]O_2$ during electrochemical cycling. *Solid State Ion.* **2012**, *207*, 44–49. [CrossRef]
102. Muhammad, S.; Lee, S.; Kim, H.; Yoon, J.; Jang, D.; Yoon, J.; Park, J.-H.; Yoon, W.-S. Deciphering the thermal behavior of lithium rich cathode material by in situ X-ray diffraction technique. *J. Power Sources* **2015**, *285*, 156–160. [CrossRef]
103. Yao, K.P.C.; Kwabi, D.G.; Quinlan, R.A.; Mansour, A.N.; Grimaud, A.; Lee, Y.-L.; Lu, Y.-C.; Shao-Horn, Y. Thermal Stability of Li_2O_2 and Li_2O for Li-Air Batteries: In Situ XRD and XPS Studies. *J. Electrochem. Soc.* **2013**, *160*, A824–A831. [CrossRef]
104. Cañas, N.A.; Einsiedel, P.; Freitag, O.T.; Heim, C.; Steinhauer, M.; Park, D.-W.; Friedrich, K.A. Operando X-ray diffraction during battery cycling at elevated temperatures: A quantitative analysis of lithium-graphite intercalation compounds. *Carbon* **2017**, *116*, 255–263. [CrossRef]
105. Kim, U.-H.; Myung, S.-T.; Yoon, C.S.; Sun, Y.-K. Extending the Battery Life Using an Al-Doped $Li[Ni_{0.76}Co_{0.09}Mn_{0.15}]O_2$ Cathode with Concentration Gradients for Lithium Ion Batteries. *ACS Energy Lett.* **2017**, *2*, 1848–1854. [CrossRef]
106. Ma, H.; Su, H.; Amine, K.; Liu, X.; Jaffer, S.; Shang, T.; Gu, L.; Yu, H. Triphase electrode performance adjustment for rechargeable ion batteries. *Nano Energy* **2018**, *43*, 1–10. [CrossRef]
107. Krumeich, F.; Waser, O.; Pratsinis, S.E. Thermal annealing dynamics of carbon-coated $LiFePO_4$ nanoparticles studied by in-situ analysis. *J. Solid State Chem.* **2016**, *242*, 96–102. [CrossRef]
108. Bleith, P.; Kaiser, H.; Novák, P.; Villevieille, C. In situ X-ray diffraction characterisation of $Fe_{0.5}TiOPO_4$ and $Cu_{0.5}TiOPO_4$ as electrode material for sodium-ion batteries. *Electrochim. Acta* **2015**, *176*, 18–21. [CrossRef]
109. Zhu, W.; Liu, D.; Trottier, J.; Gagnon, C.; Mauger, A.; Julien, C.M.; Zaghib, K. In-situ X-ray diffraction study of the phase evolution in undoped and Cr-doped $Li_xMn_{1.5}Ni_{0.5}O_4$ ($0.1 < x < 1.0$) 5-V cathode materials. *J. Power Sources* **2013**, *242*, 236–243. [CrossRef]
110. Roberts, M.R.; Madsen, A.; Nicklin, C.; Rawle, J.; Palmer, M.G.; Owen, J.R.; Hector, A.L. Direct Observation of Active Material Concentration Gradients and Crystallinity Breakdown in $LiFePO_4$ Electrodes During Charge/Discharge Cycling of Lithium Batteries. *J. Phys. Chem. C* **2014**, *118*, 6548–6557. [CrossRef] [PubMed]
111. Li, W.; Reimers, J.N.; Dahn, J.R. In situ X-ray diffraction and electrochemical studies of $Li_{1\text{-}x}NiO_2$. *Solid State Ion.* **1993**, *67*, 123–130. [CrossRef]
112. Leriche, J.B.; Hamelet, S.; Shu, J.; Morcrette, M.; Masquelier, C.; Ouvrard, G.; Zerrouki, M.; Soudan, P.; Belin, S.; Elkaïm, E.; et al. An Electrochemical Cell for Operando Study of Lithium Batteries Using Synchrotron Radiation. *J. Electrochem. Soc.* **2010**, *157*, A606. [CrossRef]
113. Lowe, M.A.; Gao, J.; Abruña, H.D. Mechanistic insights into operational lithium–sulfur batteries by in situ X-ray diffraction and absorption spectroscopy. *RSC Adv.* **2014**, *4*, 18347. [CrossRef]
114. Sasaki, T.; Villevieill, C.; Takeuchi, Y.; Novák, P. Understanding Inhomogeneous Reactions in Li-Ion Batteries: Operando Synchrotron X-ray Diffraction on Two-Layer Electrodes. *Adv. Sci.* **2015**, 1500083. [CrossRef] [PubMed]

115. Ma, R.; Shao, L.; Wu, K.; Shui, M.; Wang, D.; Pan, J.; Long, N.; Ren, Y.; Shu, J. Comparison of $LiVPO_4F$ to $Li_4Ti_5O_{12}$ as anode materials for lithium-ion batteries. *ACS Appl. Mater. Interfaces* **2013**, *5*, 8615–8627. [CrossRef] [PubMed]
116. Zhou, H.; Einarsrud, M.-A.; Vullum-Bruer, F. In situ X-ray diffraction and electrochemical impedance spectroscopy of a nanoporous Li_2FeSiO_4/C cathode during the initial charge/discharge cycle of a Li-ion battery. *J. Power Sources* **2013**, *238*, 478–484. [CrossRef]
117. Mohanty, D.; Kalnaus, S.; Meisner, R.A.; Rhodes, K.J.; Li, J.; Payzant, E.A.; Wood, D.L.; Daniel, C. Structural transformation of a lithium-rich $Li_{1.2}Co_{0.1}Mn_{0.55}Ni_{0.15}O_2$ cathode during high voltage cycling resolved by in situ X-ray diffraction. *J. Power Sources* **2013**, *229*, 239–248. [CrossRef]
118. Morcrette, M.; Chabre, Y.; Vaughan, G.; Amatucci, G.; Leriche, J.B.; Patoux, S.; Masquelier, C.; Tarascon, J.M. In situ X-ray diffraction techniques as a powerful tool to study battery electrode materials. *Electrochim. Acta* **2002**, *47*, 3137–3149. [CrossRef]
119. He, H.; Huang, C.; Luo, C.-W.; Liu, J.-J.; Chao, Z.-S. Dynamic study of Li intercalation into graphite by in situ high energy synchrotron XRD. *Electrochim. Acta* **2013**, *92*, 148–152. [CrossRef]
120. Harks, P.P.R.M.L.; Mulder, F.M.; Notten, P.H.L. In situ methods for Li-ion battery research: A review of recent developments. *J. Power Sources* **2015**, *288*, 92–105. [CrossRef]
121. Xu, F.; He, H.; Liu, Y.; Dun, C.; Ren, Y.; Liu, Q.; Wang, M.-X.; Xie, J. Failure Investigation of $LiFePO_4$ Cells under Overcharge Conditions. *J. Electrochem. Soc.* **2012**, *159*, A678–A687. [CrossRef]
122. Liu, Q.; Liu, Y.; Yang, F.; He, H.; Xiao, X.; Ren, Y.; Lu, W.; Stach, E.; Xie, J. Capacity Fading Mechanism of the Commercial 18650 $LiFePO_4$-Based Lithium-Ion Batteries: An in Situ Time-Resolved High-Energy Synchrotron XRD Study. *ACS Appl. Mater. Interfaces* **2018**, *10*, 4622–4629. [CrossRef] [PubMed]
123. Sarkar, S.; Mitra, S. Carbon Coated Submicron sized-$LiFePO_4$: Improved High Rate Performance Lithium Battery Cathode. *Energy Procedia* **2014**, *54*, 718–724. [CrossRef]
124. Zhao, N.; Li, Y.; Zhi, X.; Wang, L.; Zhao, X.; Wang, Y.; Liang, G. Effect of Ce^{3+} doping on the properties of $LiFePO_4$ cathode material. *J. Rare Earths* **2016**, *34*, 174–180. [CrossRef]
125. MacNeil, D.D.; Lu, Z.; Chen, Z.; Dahn, J.R. A comparison of the electrode/electrolyte reaction at elevated temperatures for various Li-ion battery cathodes. *J. Power Sources* **2002**, *108*, 8–14. [CrossRef]
126. Islam, M.S.; Driscoll, D.J.; Fisher, C.A.J.; Slater, P.R. Atomic-Scale Investigation of Defects, Dopants, and Lithium Transport in the $LiFePO_4$ Olivine-Type Battery Material. *Chem. Mater.* **2005**, *17*, 5085–5092. [CrossRef]
127. Allen, J.L.; Jow, T.R.; Wolfenstine, J. Kinetic Study of the Electrochemical $FePO_4$ to $LiFePO_4$ Phase Transition. *Chem. Mater.* **2007**, *19*, 2108–2111. [CrossRef]
128. Yamada, A.; Koizumi, H.; Sonoyama, N.; Kanno, R. Phase Change in Li_xFePO_4. *Electrochem. Solid-State Lett.* **2005**, *8*, A409–A413. [CrossRef]
129. Sharma, N.; Guo, X.; Du, G.; Guo, Z.; Wang, J.; Wang, Z.; Peterson, V.K. Direct Evidence of Concurrent Solid-Solution and Two-Phase Reactions and the Nonequilibrium Structural Evolution of $LiFePO_4$. *J. Am. Chem. Soc.* **2012**, *134*, 7867–7873. [CrossRef] [PubMed]
130. Yamada, A.; Koizumi, H.; Nishimura, S.-I.; Sonoyama, N.; Kanno, R.; Yonemura, M.; Nakamura, T.; Kobayashi, Y. Room-temperature miscibility gap in Li_xFePO_4. *Nat. Mater.* **2006**, *5*, 357. [CrossRef] [PubMed]
131. Chen, G.; Song, X.; Richardson, T.J. Electron Microscopy Study of the $LiFePO_4$ to $FePO_4$ Phase Transition. *Electrochem. Solid-State Lett.* **2006**, *9*, A295–A298. [CrossRef]
132. Laffont, L.; Delacourt, C.; Gibot, P.; Wu, M.Y.; Kooyman, P.; Masquelier, C.; Tarascon, J.M. Study of the $LiFePO_4$/$FePO_4$ Two-Phase System by High-Resolution Electron Energy Loss Spectroscopy. *Chem. Mater.* **2006**, *18*, 5520–5529. [CrossRef]
133. Andersson, A.S.; Kalska, B.; Häggström, L.; Thomas, J.O. Lithium extraction/insertion in $LiFePO_4$: An X-ray diffraction and Mössbauer spectroscopy study. *Solid State Ion.* **2000**, *130*, 41–52. [CrossRef]
134. Shin, H.C.; Chung, K.Y.; Min, W.S.; Byun, D.J.; Jang, H.; Cho, B.W. Asymmetry between charge and discharge during high rate cycling in $LiFePO_4$—In Situ X-ray diffraction study. *Electrochem. Commun.* **2008**, *10*, 536–540. [CrossRef]
135. Tan, H.J.; Dodd, J.L.; Fultz, B. Thermodynamic and Kinetic Stability of the Solid Solution Phase in Nanocrystalline Li_xFePO_4. *J. Phys. Chem. C* **2009**, *113*, 20527–20530. [CrossRef]
136. Li, D.; Zhou, H. Two-phase transition of Li-intercalation compounds in Li-ion batteries. *Mater. Today* **2014**, *17*, 451–463. [CrossRef]

137. Li, Z.; Yang, J.; Li, C.; Wang, S.; Zhang, L.; Zhu, K.; Wang, X. Orientation-Dependent Lithium Miscibility Gap in $LiFePO_4$. *Chem. Mater.* **2018**, *30*, 874–878. [CrossRef]
138. Wagemaker, M.; Singh, D.P.; Borghols, W.J.H.; Lafont, U.; Haverkate, L.; Peterson, V.K.; Mulder, F.M. Dynamic Solubility Limits in Nanosized Olivine $LiFePO_4$. *J. Am. Chem. Soc.* **2011**, *133*, 10222–10228. [CrossRef] [PubMed]
139. Kobayashi, G.; Nishimura, S.-I.; Park, M.-S.; Kanno, R.; Yashima, M.; Ida, T.; Yamada, A. Isolation of Solid Solution Phases in Size-Controlled Li_xFePO_4 at Room Temperature. *Adv. Funct. Mater.* **2008**, *19*, 395–403. [CrossRef]
140. Takahashi, I.; Mori, T.; Yoshinari, T.; Orikasa, Y.; Koyama, Y.; Murayama, H.; Fukuda, K.; Hatano, M.; Arai, H.; Uchimoto, Y.; et al. Irreversible phase transition between $LiFePO_4$ and $FePO_4$ during high-rate charge-discharge reaction by operando X-ray diffraction. *J. Power Sources* **2016**, *309*, 122–126. [CrossRef]
141. Liu, H.; Strobridge, F.C.; Borkiewicz, O.J.; Wiaderek, K.M.; Chapman, K.W.; Chupas, P.J.; Grey, C.P. Capturing metastable structures during high-rate cycling of $LiFePO_4$ nanoparticle electrodes. *Science* **2014**, *344*, 1252817. [CrossRef] [PubMed]
142. Cogswell, D.A.; Bazant, M.Z. Coherency Strain and the Kinetics of Phase Separation in $LiFePO_4$ Nanoparticles. *ACS Nano* **2012**, *6*, 2215–2225. [CrossRef] [PubMed]
143. Van der Ven, A.; Garikipati, K.; Kim, S.; Wagemaker, M. The Role of Coherency Strains on Phase Stability in Li_xFePO_4: Needle Crystallites Minimize Coherency Strain and Overpotential. *J. Electrochem. Soc.* **2009**, *156*, A949–A957. [CrossRef]
144. Meethong, N.; Huang, H.-Y.S.; Carter, W.C.; Chiang, Y.-M. Size-Dependent Lithium Miscibility Gap in Nanoscale Li_{1-x} $FePO_4$. *Electrochem. Solid-State Lett.* **2007**, *10*, A134–A138. [CrossRef]
145. Bai, P.; Cogswell, D.A.; Bazant, M.Z. Suppression of Phase Separation in $LiFePO_4$ Nanoparticles During Battery Discharge. *Nano Lett.* **2011**, *11*, 4890–4896. [CrossRef] [PubMed]
146. Malik, R.; Zhou, F.; Ceder, G. Kinetics of non-equilibrium lithium incorporation in $LiFePO_4$. *Nat. Mater.* **2011**, *10*, 587. [CrossRef] [PubMed]
147. Yan, M.; Zhang, G.; Wei, Q.; Tian, X.; Zhao, K.; An, Q.; Zhou, L.; Zhao, Y.; Niu, C.; Ren, W.; et al. In operando observation of temperature-dependent phase evolution in lithium-incorporation olivine cathode. *Nano Energy* **2016**, *22*, 406–413. [CrossRef]
148. Galceran, M.; Saurel, D.; Acebedo, B.; Roddatis, V.V.; Martin, E.; Rojo, T.; Casas-Cabanas, M. The mechanism of $NaFePO_4$ (de)sodiation determined by in situ X-ray diffraction. *Phys. Chem. Chem. Phys.* **2014**, *16*, 8837–8842. [CrossRef] [PubMed]
149. Moreau, P.; Guyomard, D.; Gaubicher, J.; Boucher, F. Structure and Stability of Sodium Intercalated Phases in Olivine $FePO_4$. *Chem. Mater.* **2010**, *22*, 4126–4128. [CrossRef]
150. Lu, J.; Chung, S.C.; Nishimura, S.-I.; Yamada, A. Phase Diagram of Olivine $NaxFePO_4$ ($0 < x < 1$). *Chem. Mater.* **2013**, *25*, 4557–4565. [CrossRef]
151. Chung, K.Y.; Yoon, W.-S.; Lee, H.S.; McBreen, J.; Yang, X.-Q.; Oh, S.H.; Ryu, W.H.; Lee, J.L.; Cho, W.I.; Cho, B.W. In situ XRD studies of the structural changes of ZrO_2-coated $LiCoO_2$ during cycling and their effects on capacity retention in lithium batteries. *J. Power Sources* **2006**, *163*, 185–190. [CrossRef]
152. Chung, K.Y.; Yoon, W.-S.; McBreen, J.; Yang, X.Q.; Oh, S.Y.; Shin, H.C.; Cho, W.I.; Cho, B.W. In situ X-ray diffraction studies on the mechanism of capacity retention improvement by coating at the surface of LiCoO2. *J. Power Sources* **2007**, *174*, 619–623. [CrossRef]
153. Sun, X.; Yang, X.Q.; McBreen, J.; Gao, Y.; Yakovleva, M.V.; Xing, X.K.; Daroux, M.L. New phases and phase transitions observed in over-charged states of LiCoO2-based cathode materials. *J. Power Sources* **2001**, *97–98*, 274–276. [CrossRef]
154. Chen, Z.; Dahn, J.R. Methods to obtain excellent capacity retention in LiCoO2 cycled to 4.5 V. *Electrochim. Acta* **2004**, *49*, 1079–1090. [CrossRef]
155. Ohzuku, T.; Ueda, A. Solid-State Redox Reactions of LiCoO (R3m) for 4 Volt Secondary Lithium Cells. *J. Electrochem. Soc.* **1994**, *141*, 2972–2977. [CrossRef]
156. Wang, P.-F.; You, Y.; Yin, Y.-X.; Guo, Y.-G. Layered Oxide Cathodes for Sodium-Ion Batteries: Phase Transition, Air Stability, and Performance. *Adv. Energy Mater.* **2018**, *8*, 1701912. [CrossRef]
157. Delmas, C.; Fouassier, C.; Hagenmuller, P. Structural classification and properties of the layered oxides. *Physica B+C* **1980**, *99*, 81–85. [CrossRef]

158. Yabuuchi, N.; Komaba, S. Recent research progress on iron- and manganese-based positive electrode materials for rechargeable sodium batteries. *Sci. Technol. Adv. Mater.* **2014**, *15*, 043501. [CrossRef] [PubMed]
159. Zhang, X.; Chen, Z.; Schwarz, B.; Sigel, F.; Ehrenberg, H.; An, K.; Zhang, Z.; Zhang, Q.; Li, Y.; Li, J. Kinetic characteristics up to 4.8 V of layered $LiNi_{1/3}Co_{1/3}Mn_{1/3}O_2$ cathode materials for high voltage lithium-ion batteries. *Electrochim. Acta* **2017**, *227*, 152–161. [CrossRef]
160. Yoon, W.-S.; Chung, K.Y.; McBreen, J.; Yang, X.-Q. A comparative study on structural changes of $LiCo_{1/3}Ni_{1/3}Mn_{1/3}O_2$ and $LiNi_{0.8}Co_{0.15}Al_{0.05}O_2$ during first charge using in situ XRD. *Electrochem. Commun.* **2006**, *8*, 1257–1262. [CrossRef]
161. Godbole, V.A.; Colin, J.-F.; Novak, P. Study of Overcharge Behavior of $Li_{1+x}(Ni_{1/3}Mn_{1/3}Co_{1/3})_{1-x}O_2$ Using In Situ and Ex Situ X-ray Synchrotron Diffraction. *J. Electrochem. Soc.* **2011**, *158*, A1005–A1010. [CrossRef]
162. Zhou, Y.-N.; Ma, J.; Hu, E.; Yu, X.; Gu, L.; Nam, K.-W.; Chen, L.; Wang, Z.; Yang, X.-Q. Tuning charge–discharge induced unit cell breathing in layer-structured cathode materials for lithium-ion batteries. *Nat. Commun.* **2014**, *5*, 5381. [CrossRef] [PubMed]
163. Sathiya, M.; Rousse, G.; Ramesha, K.; Laisa, C.P.; Vezin, H.; Sougrati, M.T.; Doublet, M.L.; Foix, D.; Gonbeau, D.; Walker, W.; et al. Reversible anionic redox chemistry in high-capacity layered-oxide electrodes. *Nat. Mater.* **2013**, *12*, 827. [CrossRef] [PubMed]
164. James, A.C.W.P.; Goodenough, J.B. Structure and bonding in Li_2MoO_3 and $Li_{2-x}MoO_3$ ($0 \leq x \leq 1.7$). *J. Solid State Chem.* **1988**, *76*, 87–96. [CrossRef]
165. Lu, Z.; Dahn, J.R. Can All the Lithium be Removed from T2 $Li_{2/3}[Ni_{1/3}Mn_{2/3}]O_2$? *J. Electrochem. Soc.* **2001**, *148*, A710–A715. [CrossRef]
166. Berthelot, R.; Carlier, D.; Delmas, C. Electrochemical investigation of the P2–Na_xCoO_2 phase diagram. *Nat. Mater.* **2011**, *10*, 74. [CrossRef] [PubMed]
167. Lu, Z.; Dahn, J.R. In Situ X-ray Diffraction Study of P2 $Na_{2/3}[Ni_{1/3}Mn_{2/3}]O_2$. *J. Electrochem. Soc.* **2001**, *148*, A1225–A1229. [CrossRef]
168. Wang, P.-F.; You, Y.; Yin, Y.-X.; Wang, Y.-S.; Wan, L.-J.; Gu, L.; Guo, Y.-G. Suppressing the P2–O2 Phase Transition of $Na_{0.67}Mn_{0.67}Ni_{0.33}O_2$ by Magnesium Substitution for Improved Sodium-Ion Batteries. *Angew. Chem. Int. Ed.* **2016**, *55*, 7445–7449. [CrossRef] [PubMed]
169. Han, M.H.; Gonzalo, E.; Sharma, N.; López del Amo, J.M.; Armand, M.; Avdeev, M.; Saiz Garitaonandia, J.J.; Rojo, T. High-Performance P2-Phase $Na_{2/3}Mn_{0.8}Fe_{0.1}Ti_{0.1}O_2$ Cathode Material for Ambient-Temperature Sodium-Ion Batteries. *Chem. Mater.* **2016**, *28*, 106–116. [CrossRef]
170. Xu, J.; Lee, D.H.; Clément, R.J.; Yu, X.; Leskes, M.; Pell, A.J.; Pintacuda, G.; Yang, X.Q.; Grey, C.P.; Meng, Y.S. Identifying the Critical Role of Li Substitution in P2− $Na_x[Li_yNi_zMn_{1-y-z}]O_2$ ($0 < x, y, z < 1$) Intercalation Cathode Materials for High-Energy Na-Ion Batteries. *Chem. Mater.* **2014**, *26*, 1260–1269. [CrossRef]
171. Lu, Z.; Dahn, J.R. Effects of Stacking Fault Defects on the X-ray Diffraction Patterns of T2, O2, and O6 Structure $Li_{2/3}[Co_xNi_{1/3-x}Mn_{2/3}]O_2$. *Chem. Mater.* **2001**, *13*, 2078–2083. [CrossRef]
172. Singh, G.; Tapia-Ruiz, N.; Lopez del Amo, J.M.; Maitra, U.; Somerville, J.W.; Armstrong, A.R.; Martinez de Ilarduya, J.; Rojo, T.; Bruce, P.G. High Voltage Mg-Doped $Na_{0.67}Ni_{0.3-x}Mg_xMn_{0.7}O_2$ ($x = 0.05, 0.1$) Na-Ion Cathodes with Enhanced Stability and Rate Capability. *Chem. Mater.* **2016**, *28*, 5087–5094. [CrossRef]
173. Billaud, J.; Singh, G.; Armstrong, A.R.; Gonzalo, E.; Roddatis, V.; Armand, M.; Rojo, T.; Bruce, P.G. $Na_{0.67}Mn_{1-x}Mg_xO_2$ ($0 \leq x \leq 0.2$): A high capacity cathode for sodium-ion batteries. *Energy Environ. Sci.* **2014**, *7*, 1387–1391. [CrossRef]
174. Boehm, R.C.; Banerjee, A. Theoretical study of lithium intercalated graphite. *J. Chem. Phys.* **1992**, *96*, 1150–1157. [CrossRef]
175. Ge, H.; Li, N.; Li, D.; Dai, C.; Wang, D. Study on the Theoretical Capacity of Spinel Lithium Titanate Induced by Low-Potential Intercalation. *J. Phys. Chem. C* **2009**, *113*, 6324–6326. [CrossRef]
176. Ge, H.; Li, N.; Li, D.; Dai, C.; Wang, D. Electrochemical characteristics of spinel $Li_4Ti_5O_{12}$ discharged to 0.01 V. *Electrochem. Commun.* **2008**, *10*, 719–722. [CrossRef]
177. Venkateswarlu, M.; Chen, C.H.; Do, J.S.; Lin, C.W.; Chou, T.C.; Hwang, B.J. Electrochemical properties of nano-sized $Li_4Ti_5O_{12}$ powders synthesized by a sol–gel process and characterized by X-ray absorption spectroscopy. *J. Power Sources* **2005**, *146*, 204–208. [CrossRef]

178. Shu, J. Electrochemical behavior and stability of $Li_4Ti_5O_{12}$ in a broad voltage window. *J. Solid State Electrochem.* **2009**, *13*, 1535–1539. [CrossRef]
179. Zhao, L.; Pan, H.-L.; Hu, Y.-S.; Li, H.; Chen, L.-Q. Spinel lithium titanate ($Li_4Ti_5O_{12}$) as novel anode material for room-temperature sodium-ion battery. *Chin. Phys. B* **2012**, *21*, 028201. [CrossRef]
180. Yang, L.Y.; Li, H.Z.; Liu, J.; Tang, S.S.; Lu, Y.K.; Li, S.T.; Min, J.; Yan, N.; Lei, M. $Li_4Ti_5O_{12}$ nanosheets as high-rate and long-life anode materials for sodium-ion batteries. *J. Mater. Chem. A* **2015**, *3*, 24446–24452. [CrossRef]
181. Kitta, M.; Akita, T.; Tanaka, S.; Kohyama, M. Two-phase separation in a lithiated spinel $Li_4Ti_5O_{12}$ crystal as confirmed by electron energy-loss spectroscopy. *J. Power Sources* **2014**, *257*, 120–125. [CrossRef]
182. Kitta, M.; Kuratani, K.; Tabuchi, M.; Takeichi, N.; Akita, T.; Kiyobayashi, T.; Kohyama, M. Irreversible structural change of a spinel $Li_4Ti_5O_{12}$ particle via Na insertion-extraction cycles of a sodium-ion battery. *Electrochim. Acta* **2014**, *148*, 175–179. [CrossRef]
183. Li, W.; Dahn, J.R.; Wainwright, D.S. Rechargeable Lithium Batteries with Aqueous Electrolytes. *Science* **1994**, *264*, 1115–1118. [CrossRef] [PubMed]
184. Pasta, M.; Wessells, C.D.; Huggins, R.A.; Cui, Y. A high-rate and long cycle life aqueous electrolyte battery for grid-scale energy storage. *Nat. Commun.* **2012**, *3*, 1149. [CrossRef] [PubMed]
185. Liu, J.; Xu, C.; Chen, Z.; Ni, S.; Shen, Z.X. Progress in aqueous rechargeable batteries. *Green Energy Environ.* **2018**, *3*, 20–41. [CrossRef]
186. Wang, Y.; Liu, J.; Lee, B.; Qiao, R.; Yang, Z.; Xu, S.; Yu, X.; Gu, L.; Hu, Y.-S.; Yang, W.; et al. Ti-substituted tunnel-type $Na_{0.44}MnO_2$ oxide as a negative electrode for aqueous sodium-ion batteries. *Nat. Commun.* **2015**, *6*, 6401. [CrossRef] [PubMed]
187. Wang, Y.; Yu, X.; Xu, S.; Bai, J.; Xiao, R.; Hu, Y.-S.; Li, H.; Yang, X.-Q.; Chen, L.; Huang, X. A zero-strain layered metal oxide as the negative electrode for long-life sodium-ion batteries. *Nat. Commun.* **2013**, *4*, 2365. [CrossRef] [PubMed]
188. Köhler, J.; Makihara, H.; Uegaito, H.; Inoue, H.; Toki, M. LiV_3O_8: Characterization as anode material for an aqueous rechargeable Li-ion battery system. *Electrochim. Acta* **2000**, *46*, 59–65. [CrossRef]
189. Wu, J.; Gao, X.; Yu, H.; Ding, T.; Yan, Y.; Yao, B.; Yao, X.; Chen, D.; Liu, M.; Huang, L. A Scalable Free-Standing V_2O_5/CNT Film Electrode for Supercapacitors with a Wide Operation Voltage (1.6 V) in an Aqueous Electrolyte. *Adv. Funct. Mater.* **2016**, *26*, 6114–6120. [CrossRef]
190. Yamada, Y.; Usui, K.; Sodeyama, K.; Ko, S.; Tateyama, Y.; Yamada, A. Hydrate-melt electrolytes for high-energy-density aqueous batteries. *Nat. Energy* **2016**, *1*, 16129. [CrossRef]
191. Wang, H.; Huang, K.; Zeng, Y.; Yang, S.; Chen, L. Electrochemical properties of TiP_2O_7 and $LiTi_2(PO_4)_3$ as anode material for lithium ion battery with aqueous solution electrolyte. *Electrochim. Acta* **2007**, *52*, 3280–3285. [CrossRef]
192. Wu, M.-S.; Wang, M.-J.; Jow, J.-J.; Yang, W.-D.; Hsieh, C.-Y.; Tsai, H.-M. Electrochemical fabrication of anatase TiO_2 nanostructure as an anode material for aqueous lithium-ion batteries. *J. Power Sources* **2008**, *185*, 1420–1424. [CrossRef]
193. Wang, Y.; Yang, S.-Z.; You, Y.; Feng, Z.; Zhu, W.; Gariépy, V.; Xia, J.; Commarieu, B.; Darwiche, A.; Guerfi, A.; Zaghib, K. High-Capacity and Long-Cycle Life Aqueous Rechargeable Lithium-Ion Battery with the $FePO_4$ Anode. *ACS Appl. Mater. Interfaces* **2018**, *10*, 7061–7068. [CrossRef] [PubMed]
194. Dai, H.; Yang, C.; Ou, X.; Liang, X.; Xue, H.; Wang, W.; Xu, G. Unravelling the electrochemical properties and thermal behavior of $NaNi_{2/3}Sb_{1/3}O_2$ cathode for sodium-ion batteries by in situ X-ray diffraction investigation. *Electrochim. Acta* **2017**, *257*, 146–154. [CrossRef]
195. Same, A.; Park, J.W.; Battaglia, V.; Tang, H.Y. In situ neutron radiography analysis of graphite/NCA lithium-ion battery during overcharge. *J. Appl. Electrochem.* **2012**, *42*, 1–9. [CrossRef]
196. Lu, W.; López, C.M.; Liu, N.; Vaughey, J.T.; Jansen, A.; Dennis, W.D. Overcharge Effect on Morphology and Structure of Carbon Electrodes for Lithium-Ion Batteries. *J. Electrochem. Soc.* **2012**, *159*, A566–A570. [CrossRef]

197. Makimura, Y.; Sasaki, T.; Oka, H.; Okuda, C.; Nonaka, T.; Nishimura, Y.F.; Kawauchi, S.; Takeuchi, Y. Studying the Charging Process of a Lithium-Ion Battery toward 10 V by In Situ X-ray Absorption and Diffraction: Lithium Insertion/Extraction with Side Reactions at Positive and Negative Electrodes. *J. Electrochem. Soc.* **2016**, *163*, A1450–A1456. [CrossRef]
198. Patterson, A.L. The Scherrer Formula for X-ray Particle Size Determination. *Phys. Rev.* **1939**, *56*, 978–982. [CrossRef]
199. Ziolkowska, D.A.; Jasinski, J.B.; Hamankiewicz, B.; Korona, K.P.; Wu, S.-H.; Czerwinski, A. In Situ XRD and TEM Studies of Sol-Gel-Based Synthesis of LiFePO$_4$. *Cryst. Growth Des.* **2016**, *16*, 5006–5013. [CrossRef]